

Search for very-high-energy gamma-ray counterparts to IceCube neutrino events using VERITAS

Samuel Trépanier

Master of Science

Department of Physics

McGill University

Montreal, Quebec

2018-03-12

A thesis submitted to McGill university in partial fulfillment of the requirements for the degree of Master of Science

©Samuel Trépanier, 2018

ACKNOWLEDGEMENTS

First and foremost, I would like to thank my supervisor, Prof. Ken Ragan, for his continuing support and thoughtful advice throughout my master study and research. I am so thankful for him taking the time to meet individually once a week. These sessions have been very constructive and helped guiding me in the right direction. Thanks to my friend Benoit Lefebvre for encouraging me to apply for graduate studies and his very precious help over the last two years. I would also like to thank Prof. David Hanna and my colleagues Andrew McCann, Qi Feng, Benjamin Zitzer, Sean Griffin, Simon Archambault, Jonathan Tyler, Tony Lin, Étienne Bourbeau and Gabriel Chernitsky for making this research group feel like a family. Special thanks to Marcos Santander and Ava Ghadimi from Columbia University for suggesting this project and helping me out with the analysis. Many thanks to Paul Mercure and Juan Gallego for providing technical assistance with the computer network. Thanks to all my family and friends for being there for me during the good times, the bad and everything in-between. Finally, I would like to thank Kommiee for her love, patience and encouragements and my mother, my father and my brother for their unconditional love and support.

ABSTRACT

The IceCube South Pole Neutrino Observatory consists of an array of ~ 5600 photodetectors distributed within a cubic kilometre of ice ranging between 1.5 to 2.5 km in depth. This configuration allows the detection of the Cherenkov light produced by the passage of high-energy charged particles resulting from neutrino interactions. In 2013, the IceCube collaboration announced the discovery of a high-energy astrophysical neutrino flux for the first time, opening a new window for the exploration of the high-energy universe. Astrophysical neutrinos are thought to be produced from the decay of charged pions coming from hadronic interactions and are expected to be accompanied by gamma rays produced by the decay of the neutral pions. Consequently, in the same year, the VERITAS gamma-ray observatory, in Arizona, initiated its multimessenger program with the main goal of searching for a gamma-ray counterpart to the neutrino events found by IceCube. VERITAS is composed of four 12-meter telescopes that image the Cherenkov light emitted from the passage of the electromagnetic cascade in air produced by the interaction of gamma rays high in the atmosphere. This thesis describes the results from VERITAS' search for a gamma-ray counterpart to IceCube neutrino events. No gamma-ray sources were found in the regions corresponding to the arrival directions of IceCube neutrino events. On the other hand, calculations of flux upper limits constrain the gamma-ray flux to be less than $\sim 10\%$ Crab. Future gamma-ray experiments with better sensitivity, such as CTA, will allow better performance for follow-up observations.

ABRÉGÉ

L'Observatoire de neutrinos IceCube, situé en Antarctique, consiste en un réseau de ~ 5600 photodétecteurs distribués dans un volume d'un kilomètre cube de glace à une profondeur allant de 1,5 à 2,5 kilomètres. Cette configuration rend possible la détection du rayonnement Tcherenkov produit par le passage de particules chargées de hautes énergies créées résultant de l'interaction de neutrinos. En 2013, la collaboration IceCube a annoncé la découverte d'un flux de neutrinos cosmiques, ouvrant ainsi une nouvelle fenêtre sur l'astrophysique des hautes énergies. Les neutrinos astrophysiques sont produits lors de la désintégration de pions chargés provenant d'interactions hadroniques et devraient normalement être accompagnés par des rayons gamma produits par la désintégration des pions neutres. Par conséquent, la même année, l'observatoire de rayons gamma VERITAS, en Arizona, a démarré son programme d'astronomie multimessager avec comme but principal de chercher une contrepartie gamma aux événements de neutrinos découverts par IceCube. VERITAS est composé de quatre télescopes de 12 mètres de diamètre qui imagent la lumière Tcherenkov émise par le passage de la cascade électromagnétique dans l'air causée par l'interaction de rayons gamma en haute atmosphère. Ce mémoire décrit les résultats des efforts faits par VERITAS afin de trouver une contrepartie gamma aux événements neutrinos d'IceCube. Aucune source de rayons gamma n'a été trouvée dans les régions correspondant aux directions d'arrivée des événements neutrinos d'IceCube. D'un autre côté, des calculs de limites supérieures de flux contraignent les flux de rayons gamma à des valeurs inférieures à $\sim 10\%$ Crab. Les futures

expériences de rayons gamma, tel CTA, auront une meilleure sensibilité et seront donc plus performantes pour effectuer des observations de suivi.

TABLE OF CONTENTS

ACKNOWLEDGEMENTS	ii
ABSTRACT	iii
ABRÉGÉ	iv
LIST OF TABLES	viii
LIST OF FIGURES	ix
1 Introduction	1
1.1 Multimessenger astronomy	1
1.2 Thesis overview	2
2 High energy astrophysics	4
2.1 Cosmic ray acceleration	5
2.2 Gamma-ray and neutrino production	6
2.3 TeV sources	7
2.3.1 Galactic	7
2.3.2 Extragalactic	9
3 IceCube experiment	11
3.1 IceCube Array	12
3.1.1 Digital Optical Modules	12
3.1.2 Main detector	15
3.1.3 DeepCore	16
3.1.4 IceTop	16
3.1.5 IceCube Lab	16
3.2 Detection	17
3.2.1 Neutrino event signatures	18
3.2.2 Starting events	19

3.2.3	Through-going muons	20
3.3	Combined results	21
4	VERITAS experiment	26
4.1	Imaging Atmospheric Cherenkov Telescope	26
4.1.1	History	27
4.1.2	Imaging Technique	29
4.2	Instrument	29
4.2.1	Telescopes	32
4.2.2	Camera	32
4.2.3	Data acquisition	34
4.2.4	Calibration	35
4.3	Analysis technique	36
4.3.1	Image cleaning	37
4.3.2	Parameterization	37
4.3.3	Event reconstruction	39
4.3.4	Gamma/hadron separation	41
4.3.5	Significance and skymap	44
4.3.6	Flux and upper limit	45
5	VHE gamma ray counterparts to IceCube neutrinos	49
5.1	Event selection	49
5.2	Observation summary	51
5.3	Significance	52
5.4	Upper limit	55
6	Conclusion	58
6.1	Summary	58
6.2	Discussion	58
6.3	Future work	59
A	Significance maps and distribution	60
B	Flux upper limit spectra	68
	References	73

LIST OF TABLES

<u>Table</u>	<u>page</u>
3-1 Hamamatsu specifications for the R7081-02 PMT (typical).	14
4-1 The main Hillas parameters for a single telescope that are still in use in stereoscopic arrays.	40
4-2 Summary: VEGAS regular soft cuts for nominal (reduced) HV.	41
5-1 IceCube high-energy starting event (HESE) positions compared with VERITAS pointing.	50
5-2 IceCube through-going muon event positions from 2-year and 6-year data compared with VERITAS pointing	50
5-3 List of IceCube high energy events observed by VERITAS with the observation time, in minutes, on each source.	53
5-4 Summary of the results from the point source analysis of the IceCube events follow-up data observed by VERITAS, after subtraction of the Reduced HV large wobble offset data as mentioned in the text. .	56

LIST OF FIGURES

<u>Figure</u>	LIST OF FIGURES	<u>page</u>
2-1	All-particle cosmic-ray spectrum as a function of energy (energy per nucleus) from air shower measurements.	5
2-2	VHE gamma-ray skymap showing galactic and extra-galactic sources of gamma-rays in the VHE energy range.	8
3-1	Schematic view of the IceCube In-Ice Array, showing to scale the different components of the detector.	13
3-2	Schematic view of the different components of an IceCube DOM. . . .	14
3-3	The deployment of a string of PMTs in the ice.	15
3-4	The IceCube Laboratory, March 2015.	17
3-5	Simulated Cherenkov photons for the two main neutrino interactions in Antarctic ice.	19
3-6	Arrival direction of the 54 “starting neutrino event” candidates found in four years of data.	20
3-7	Equatorial skymap showing the arrival directions and energies of the 29 most energetic up-going muon track events with energy higher than 200 TeV.	21
3-8	Event view of the PeV event muon track inside the detector.	22
3-9	All-sky map of the negative logarithm of the pre-trial p-value assuming no clustering as the null-hypothesis.	24
3-10	Spectrum of the combined analysis of extra-solar neutrino candidates found by IceCube.	25
4-1	The VERITAS array and buildings in September 2009.	27

4-2	Depiction of the Cherenkov emission from an air shower and its detection on the ground by an IACT array.	28
4-3	Monte Carlo simulations of the charged particle tracks in air showers caused by a 100 GeV photon and a 100 GeV proton entering the atmosphere.	30
4-4	Photograph of Telescope 4 observing under moonlight with its different components indicated.	31
4-5	<i>Left:</i> Photograph of the Photonis XP 2970 and Hamamatsu R10560-100-20 PMTs. <i>Right:</i> Picture of the camera with the light cones installed onto the PMTs.	33
4-6	Quantum efficiency of the previous PMTs used by VERITAS, compared to the new ones as a function of the wavelength.	34
4-7	FADC trace produced by the Cherenkov light from a cosmic ray air shower as shown in a single channel.	36
4-8	Different steps of the image cleaning method.	38
4-9	Main Hillas parameters for a single telescope.	39
4-10	A simulated gamma-ray shower, as seen by the telescopes after image cleaning.	42
4-11	All four images taken by the telescopes projected onto the camera plane and on the ground.	43
4-12	Illustration of the wobble observation mode as well as the reflected region technique.	45
4-13	Skymap of the Crab nebula as obtained by VEGAS analysis of approximately 80 minutes exposure time data.	46
4-14	Significance distributions for the same Crab nebula data analysis shown in figure 4-13.	47
5-1	Significance map and significance distribution of the IceCube event IC_NU20, which corresponds to the event ID 27 as published in [5].	54

5-2	Spectrum of gamma-ray flux upper limits coming from the direction of the IceCube PeV neutrino event IC_NU20.	57
-----	---	----

CHAPTER 1

Introduction

1.1 Multimessenger astronomy

The discovery of cosmic rays at the beginning of the 20th century was the first glimpse of the high energy universe. Several decades later, balloon and spacecraft experiments detected astrophysical gamma rays. In 1989, gamma radiation in the TeV range was discovered by the Whipple Observatory at Mount Hopkins, in Arizona, using the imaging atmospheric Cherenkov technique (see section 4.1). The recent discoveries of astrophysical neutrinos by IceCube and gravitational waves by LIGO open new windows for the exploration of high-energy astrophysical phenomena.

Together, gamma rays, cosmic rays, neutrinos and gravitational waves, give complementary information about the high-energy processes happening in the universe. The new detection of the GW170817 gravitational wave event by LIGO [13] is a great example of the power of this multimessenger approach. The signal, produced by the inspiral and merger of a neutron star binary system, correlates with the observation of a short gamma-ray burst by Fermi and Integral space telescopes and an optical transient in the galaxy NGC 4996 by multiple telescopes from radio to X-ray wavelengths [13].

One of the biggest mysteries of modern astrophysics remains the origin of the ultra-high energy cosmic rays (UHE, $E > 10^{18}$ eV) such as the ones detected by the

Pierre Auger Observatory [18], in Argentina. As cosmic rays propagate, their interactions with the interstellar medium are expected to emit gamma rays and, in some scenarios, neutrinos. The correlation between different messengers can contribute greatly to our understanding of these processes.

1.2 Thesis overview

The VERITAS gamma-ray observatory multimessenger program is primarily focussed on the study of the connection between very-high-energy gamma rays and the astrophysical neutrino flux discovered by the IceCube telescope. In this thesis, the efforts and results of the VERITAS search for a gamma-ray counterpart to the IceCube neutrino events are presented.

Chapter 2 contains a brief introduction to high-energy astrophysics with a focus on the cosmic-ray acceleration processes and the gamma-ray and neutrino production mechanisms. This is followed by a brief overview of the main gamma-ray and possible neutrino astrophysical sources, both galactic and extragalactic.

Chapter 3 describes the IceCube South Pole Neutrino Observatory detector and gives an overview of the results from the analysis of more than 6 years of data.

Chapter 4 describes the Imaging Atmospheric Cherenkov Telescope (IACT) technique, followed by a more detailed description of the VERITAS gamma-ray observatory instrument, data acquisition and analysis technique.

Chapter 5 describes the IceCube neutrino events that were selected to be followed-up by VERITAS to look for a gamma-ray counterpart and gives a summary of the observations. The results of the analysis are also presented.

Chapter 6 provides a summary of the results obtained and describes possible future work.

All figures from third parties used in this thesis are referenced and used with permission.

CHAPTER 2

High energy astrophysics

Cosmic rays are charged particles which are accelerated to energies that can reach the very-high energy range (VHE, $E > 100$ GeV). Since their discovery by Victor Hess at the beginning of the 20th century [32], the origin of the ultra-high energy (UHE) cosmic rays remains a mystery. They are the highest-energy particles known to exist in the universe with energies measured up to 10^{20} eV (100 EeV) [28]. Figure 2–1 shows the all-particle cosmic ray spectrum as a function of energy. The great majority of the cosmic radiation penetrating the Earth’s atmosphere is composed of atomic nuclei that were stripped of their electrons and a smaller fraction are other charged particles such as electrons or antimatter (positrons and antiprotons). Of the cosmic-ray nuclei, 79% are free protons and 15% are alpha particles, the remaining being the nuclei of heavier elements [33]. Multiple models of the astrophysical processes involved in cosmic ray acceleration exist and different galactic and extragalactic objects are candidate sources of cosmic rays. These will be briefly discussed later in this chapter. A difficulty encountered in the study of cosmic rays is the deviation of the trajectory of these charged particles as they are travelling through the interstellar and intergalactic medium, combined with the poor knowledge of the galactic and extra-galactic magnetic fields. Consequently, the cosmic rays do not generally point to the location where they originated. However, as cosmic rays travel through a medium, they interact with other particles, producing gamma-rays and

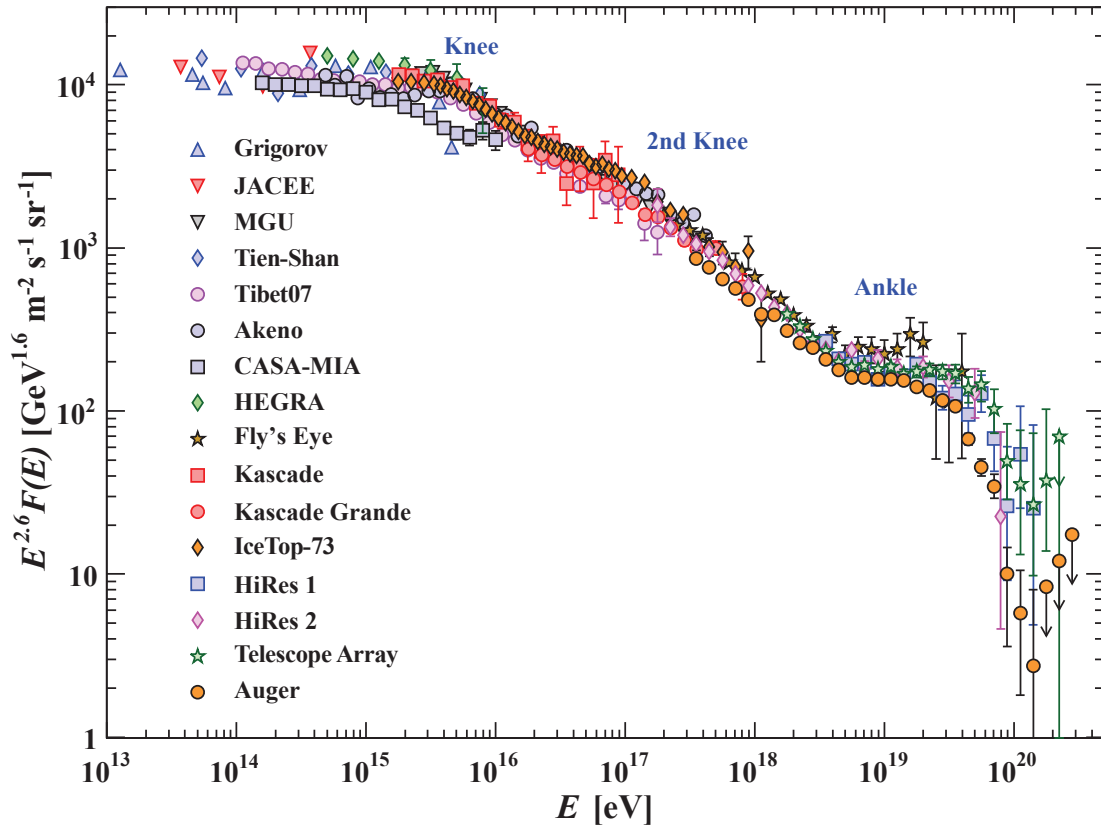


Figure 2–1: All-particle cosmic-ray spectrum as a function of energy (energy per nucleus) from air shower measurements. Figure taken from [33].

neutrinos. These secondary particles are unaffected by magnetic fields and therefore, travel in straight lines. High energy astrophysical gamma-rays and neutrinos are then unique probes to understand the origin of the highest-energy particles of our universe.

2.1 Cosmic ray acceleration

The acceleration of charged particles to the non-thermal energy at which cosmic rays are observed can be explained by a variety of mechanisms. Many of them come

from a derivation that was first published by Enrico Fermi in 1949 and are known as Fermi acceleration mechanisms. Fermi acceleration occurs in a collisionless environment where particles are repeatedly reflected, usually by a magnetic mirror, each time gaining energy. Fermi acceleration mechanisms in shocks are so-called first-order types since the energy gain at each shock crossing is proportional to $\beta_s = v_s/c$, where v_s is the shock velocity. In the environment of a moving gas cloud, Fermi acceleration mechanisms are of second-order types, since the mean energy gain per bounce is proportional to $\beta_c^2 = (v_c/c)^2$, where v_c is the cloud velocity. Examples of first-order Fermi type mechanisms are diffuse shock acceleration and magnetic reconnection acceleration. Stochastic or turbulent acceleration is an example of second-order Fermi type mechanism. Other promising mechanisms include electrostatic type acceleration (ex: pulsar) and wake field acceleration. See Appendix of [30] for a more detailed description of cosmic ray acceleration mechanisms.

2.2 Gamma-ray and neutrino production

As cosmic rays propagate through a medium, they may undergo hadronic interactions with protons, neutrons and photons (pp , pn , $p\gamma$). As a result, there is production of mesons, mostly charged and neutral pions (π^\pm , π^0). The charged pions then decay as follows:

$$\begin{aligned}\pi^+ &\rightarrow \mu^+ + \nu_\mu \\ \mu^+ &\rightarrow e^+ + \nu_e + \bar{\nu}_\mu\end{aligned}\tag{2.1}$$

$$\begin{aligned}\pi^- &\rightarrow \mu^- + \bar{\nu}_\mu \\ \mu^- &\rightarrow e^- + \bar{\nu}_e + \nu_\mu\end{aligned}\tag{2.2}$$

producing neutrinos, while the neutral pions decay as follows:

$$\pi^0 \rightarrow \gamma + \gamma \tag{2.3}$$

producing gamma-rays.

Hadronic interactions are then expected to produce both neutrinos and gamma-rays. Gamma-rays are also expected to be produced in electromagnetic interactions, mainly inverse-Compton scattering, which occurs when lower-energy photons are scattered to higher energies by relativistic electrons. In this latter process, no neutrino counterparts are expected. Therefore, while gamma-ray sources are not necessarily expected to emit neutrinos, neutrino sources are expected to have gamma-ray counterparts.

2.3 TeV sources

Various astrophysical objects in the Universe are known to be cosmic-ray accelerators as they are VHE gamma-ray emitters. Therefore, those objects are also candidates for the emission of astrophysical neutrinos. In the present section, the main galactic sources, namely supernova remnants, pulsars and compact binary systems, followed by the main extragalactic sources, active galactic nuclei and gamma ray bursts, will be briefly described. Figure 2–2 shows the most recent TeV gamma-ray sky map along with the most probable source association.

2.3.1 Galactic

Supernovas are catastrophic explosions of stars. Although a supernova only lasts for a short time ($\mathcal{O}(s)$), the supernova remnant (SNR) can emit strong electromagnetic radiation for up to $\sim 100\,000$ years. The shock wave of a SNR is an example of a

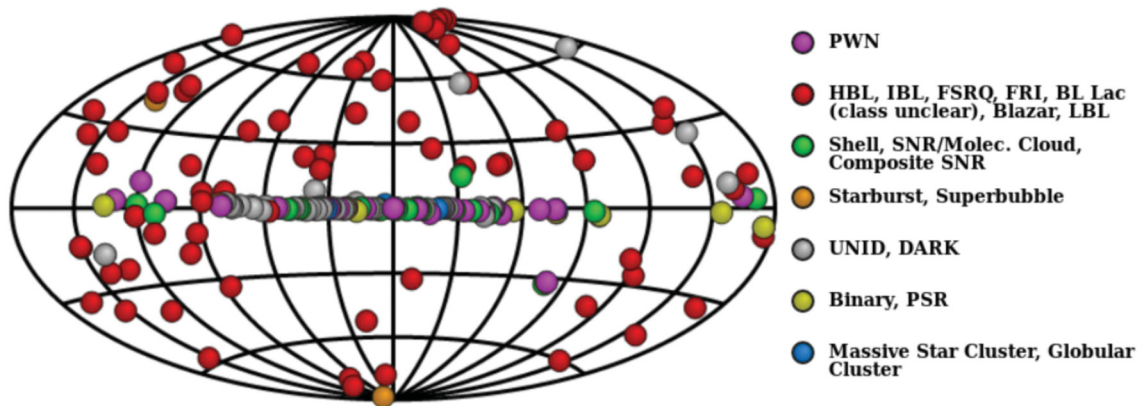


Figure 2–2: VHE gamma-ray skymap showing galactic and extra-galactic sources of gamma-rays in the VHE energy range. The legend indicates the most probable nature of the source. As can be seen, the galactic sources (purple, green, yellow and blue) are mostly concentrated in the galactic disc, while the extragalactic sources (red and orange) are isotropic in origin. Many sources are also unidentified (grey). Figure taken from [37].

place where particles are accelerated to relativistic velocities via Fermi acceleration. The debate on the leptonic versus hadronic origin of gamma rays from SNR is still open [21] and therefore the emission of neutrinos is plausible.

Pulsars are rapidly rotating neutron stars, the stellar remnants of a parent star of approximately 10 to 25 solar masses left after the supernova explosion. Strong magnetic fields at both poles of the neutron star¹ accelerate particles to cosmic-ray energies, powering the supernova remnant. These objects are known as pulsar wind

¹ The magnetic poles of a neutron star don't necessarily match the rotational poles. Therefore as the neutron star rotates, a lighthouse effect can be observed, giving rise to a pulsation of period ranging from milliseconds to a few seconds.

nebula (PWN). Most of the theoretical models predict that the particles accelerated in PWN are electrons and positrons. However, some other models propose hadronic acceleration [34]. The detection of neutrinos would be a “smoking gun” for these theories.

Compact binary systems are combinations of a compact object (white dwarf, neutron star or black hole) gravitationally bound to a star. As mass is transferred from the star to the compact object, particle acceleration occurs leading to the emission of high-energy radiation, in some cases up to VHE gamma rays. A microquasar is a subcategory of compact binary for which a black hole with a mass several times that of the sun accretes matter from a companion star. Again, both leptonic and hadronic gamma ray scenarios can be expected from compact binaries [36].

2.3.2 Extragalactic

While some galactic sources are thought to be candidates for high energy neutrino emission, the flux detected by IceCube appears to be isotropic. The Galactic contribution to the diffuse neutrino flux was constrained to less than 14% of the total neutrino flux detected by IceCube [7]. Consequently, extragalactic sources are better prospects for the origin of the high energy neutrinos discovered by IceCube.

Active galactic nuclei (AGNs) are galaxies harbouring a supermassive black hole in their nucleus which is actively accreting matter. This accretion powers bright jets that can be detectable in radio, optical, X-rays or γ -rays. Models of AGNs’ electromagnetic emission can be classified as leptonic, hadronic or lepto-hadronic type, based on the dominant component of the observed spectrum. Radio-loud AGNs,

especially blazars², were the earliest and remain a serious candidate of cosmic ray accelerators [30]. As the jets plow into the intergalactic medium, they undergo shocks and are ideal sites for the acceleration of protons. They could then be the source of the UHE cosmic-rays observed as well as the high-energy gamma-rays. An additional consequence to this would be the emission of VHE neutrinos.

Gamma-ray bursts (GRBs) constitute the most energetic explosions in the universe. They are detected when spacecraft such as Fermi or Swift trigger on an initial prompt γ -ray emission lasting milliseconds to tens of minutes, over the range of 0.1 to 10 MeV, and sometimes up to ~ 100 GeV [30]. GRBs lasting less than 2 seconds are referred to as short GRBs and are thought to be caused by the merger of degenerate compact binaries. On the other hand, those lasting more than 2 seconds are called long GRBs and are associated with the core collapse of massive stars. These result in highly relativistic jets which emerge from the collapsing or merging progenitor system. The non-thermal emission of GRBs is generally associated with synchrotron radiation and inverse Compton scattering of Fermi-accelerated electrons at the shock region, where the jets meet the external medium. Other alternative mechanisms have been proposed leading to the acceleration of protons, which would lead to MeV to EeV neutrinos [30].

² Blazars are a rare sub-class of radio-loud AGNs whose jets point close to the line of sight.

CHAPTER 3

IceCube experiment

The IceCube South Pole Neutrino Observatory is a neutrino experiment located at the South Pole ice cap, in Antarctica. It consists of an array of over 5000 photomultiplier tubes (PMTs) distributed within a cubic kilometre of ice at a depth ranging from 1.5 to 2.5 km. High energy neutrino interactions in Earth or in the ice result in the emission of relativistic secondary charged particles. As these secondary particles pass through the ice, Cherenkov light is emitted, which can be detected by IceCube's PMTs. The construction of the observatory took seven years, from 2004 to 2010 and the commissioning was completed in 2011. In 2013, the IceCube experiment announced the first discovery¹ of extra-solar neutrinos, from the analysis of 2 years of data. The large detection volume is the main advantage of IceCube because neutrinos have an extremely small interaction cross-section. Furthermore, ice has great optical properties which makes it a suitable medium for the propagation of

¹ Except for Supernova 1987A, a core-collapse supernova which occurred in the large Magellanic Cloud. Approximately three hours before visible light from the supernova reached the Earth, neutrino detections were reported by three different neutrino detectors in Japan, United States and Russia [15, 16, 24]. Despite this discovery being of great interest, it consists of a rare, isolated phenomenon.

Cherenkov light. In this chapter, the different components of the IceCube observatory will be described. The data analysis will then be briefly discussed, followed by a summary of the detected event candidates.

3.1 IceCube Array

The light detectors used by IceCube to detect Cherenkov light are 25-cm PMTs encapsulated into pressurized spheres along with some electronics, forming the Digital Optical Modules (DOMs). In total, 5160 DOMs are distributed in the cubic kilometre of ice, deployed as 86 strings of 60 DOMs at depths of 1450 m to 2450 m. Figure 3–1 shows a schematic view of the IceCube detector array. The detector is divided into three main sections: the main array, DeepCore and IceTop. At the surface lies the IceCube Lab, containing the readout computers.

3.1.1 Digital Optical Modules

The DOMs are the fundamental constituents of the IceCube observatory. They consist of glass spheres of 33 cm diameter which contain a downward-facing 25-cm PMT along with its electronics. Figure 3–2 shows the different components of an IceCube DOM. The PMTs used by IceCube are the R7081-02, made by Hamamatsu Photonics. They were chosen for their low dark noise and good time and charge resolution for single photons. Their spectral response ranges from 200-650 nm, with a maximum quantum efficiency of 25% at 390 nm [10]. The R7081-02 PMTs contain 10 linear focused dynodes and require a supplied voltage of 1500 V to achieve a nominal gain of 10^7 . At nominal gain, the single electron pulse corresponds to a signal of ~ 8 mV, which is well above the digitizer precision and other noise levels

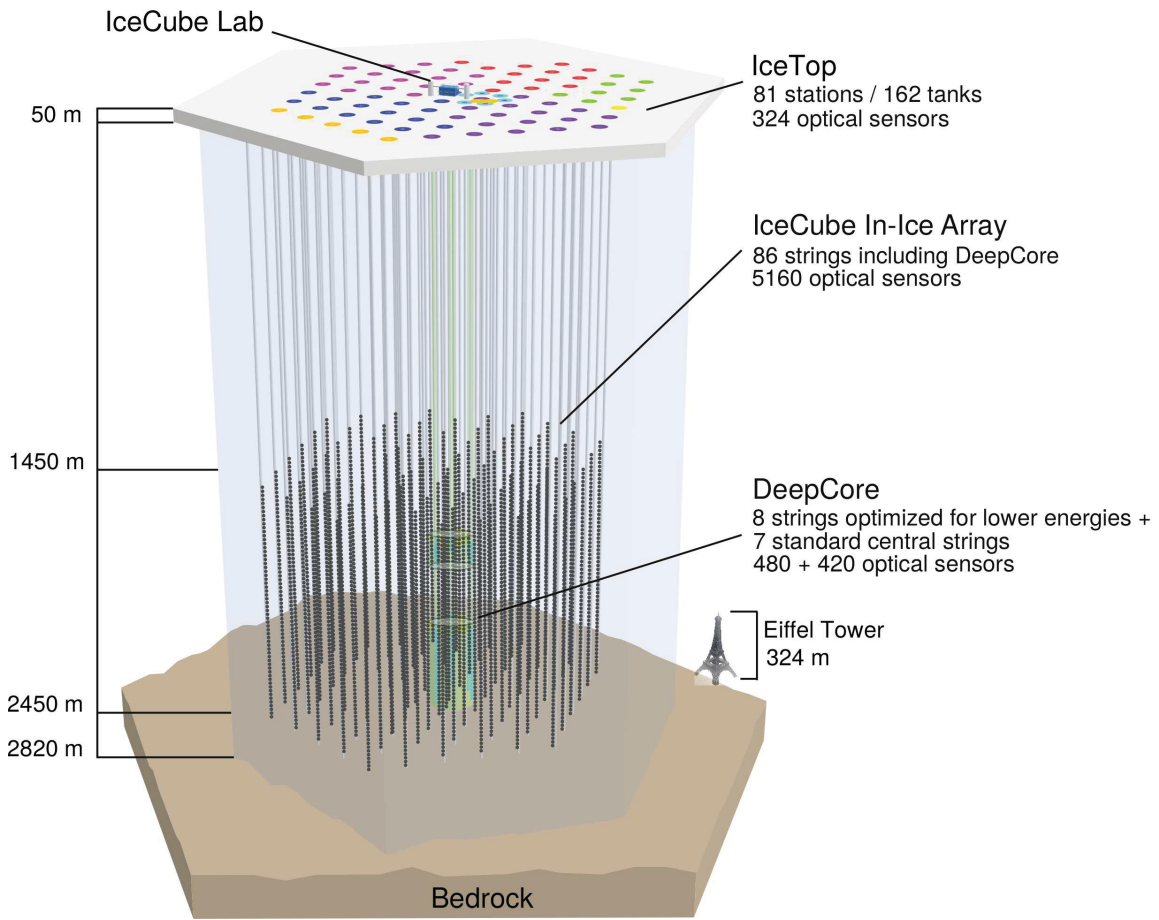


Figure 3–1: Schematic view of the IceCube array [10], showing to scale the different components of the detector.

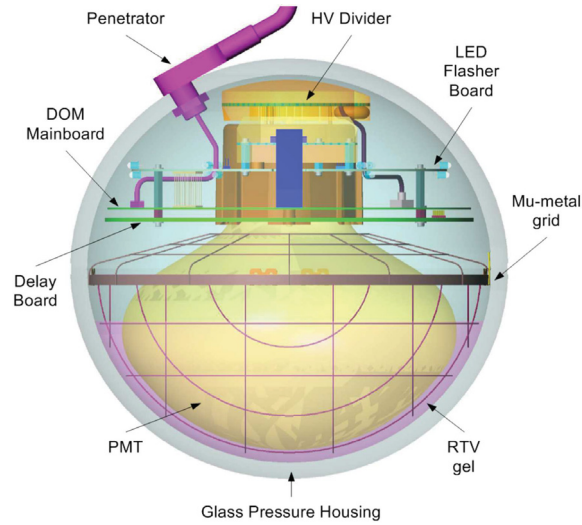


Figure 3–2: Schematic view of the different components of an IceCube DOM [11]

Table 3–1: Hamamatsu specifications for the R7081-02 PMT (typical) [12].

Spectral response	300 to 650 nm
Quantum efficiency at 390 nm	25%
Supply voltage for gain 10^7	1500 V
Dark rate at -40°C	500 Hz
Transit time spread	3.2 ns
Peak to valley ratio for single photons	2.5
Pulse linearity at 2% deviation	70 mA

(~ 0.1 mV) [12]. Table 3–1 shows some manufacturer’s specification of the R7081-02 PMT. Around the neck of the PMT lies the main board, which provides data acquisition, control, calibration and communication [10]. The PMT high voltage is generated by a different circuit board. Each DOM also contains an LED flasher board which generates light used for calibration purposes.



Figure 3–3: The deployment of a string of PMTs in the ice [17]. Each of the 86 holes were dug using a hot water drill. The average time required for drilling and reaming a 2500-meter hole was 30 hours. The holes had a diameter of approximately 60 cm and a lifetime of 24 hours before closure from refreezing. The insertion of the string of PMTs under the ice then required approximately 11 hours.

3.1.2 Main detector

The main detector consists of 78 strings distributed on a triangular grid with a horizontal spacing of 125 meters [10]. The whole array has a hexagonal shape and covers an area of a square kilometre. The vertical spacing between each of the 60 DOMs carried by each of the strings is 17 meters; the strings extend over a kilometre in length. The strings were inserted in the ice using a high pressure hot water drill. Figure 3–3 shows photographs of strings being inserted into the ice. This specific design instruments a cubic kilometre of ice and provides IceCube with the ability to detect astrophysical neutrinos of energies ranging from $\mathcal{O}(\text{TeV})$ to $\mathcal{O}(\text{PeV})$ [10].

3.1.3 DeepCore

In order to extend the energy range toward lower energies, 8 additional strings are located in the centre region of IceCube. These strings also contain 60 DOMs, but they are deployed at a greater depth and are more closely distributed, forming the DeepCore. The horizontal spacing between DeepCore's strings varies from 41 m to 105 m with an average of 72 m [10]. The 50 deepest DOMs are only 7 m apart and are concentrated between 2100 and 2450 m deep. The remaining 10 DOMs are placed at a depth shallower than 2000 metres with a vertical spacing of 10 m and act as a veto layer to reject downgoing atmospheric muons. This DeepCore configuration enables IceCube to detect neutrinos with energy ranging from 10 GeV to 100 GeV [10].

3.1.4 IceTop

IceTop consists of a surface detector, 1450 meters over the IceCube in-ice array. It is composed of 81 stations of two ice tanks separated from each other by 10 m and containing two DOMs each, identical to the ones in the IceCube array. The spacing between stations approximately follow the spacing of the in-ice array's strings with a denser region over DeepCore. The IceTop array is mainly dedicated to cosmic ray astronomy, observing the products of high energy cosmic rays interacting in the atmosphere. It also acts as a veto, in order to reduce the atmospheric muon background produced by cosmic ray interactions.

3.1.5 IceCube Lab

The IceCube Laboratory is the central operations centre of the IceCube experiment. It consists of a two-storey building located at the surface of the ice, centred on the array (Figure 3–4). The whole building is maintained at a temperature of 18°C to



Figure 3–4: The IceCube Laboratory, March 2015 [17].

prevent overheating. Two cable towers connect the in-ice array to the readout computers on the second floor, which are shielded against electromagnetic interference. The IceCube Laboratory’s power is supplied by the South Pole Station generator [10].

3.2 Detection

The main background to the IceCube search for astrophysical neutrinos is muons and atmospheric neutrinos produced in the interaction of cosmic rays in Earth’s atmosphere. Despite IceCube being 1.5 km under the ice, the cosmic ray-induced atmospheric muons trigger the IceCube detector at an average rate of 2.7 kHz [9]. One way to reduce this background is to require the neutrino to interact within the detector, using the outer layers as a veto. Another way is to only keep the up-going muons coming from the northern hemisphere and using the Earth as a shield. This latter method allows the neutrinos to interact outside of the detector, increasing the effective area. The atmospheric neutrinos remain an irreducible background to the

astrophysical neutrinos, triggering the detector at 20 mHz [9]. However, differences in the energy spectra of atmospheric and astrophysical neutrinos can be used to separate the signal from the background.

3.2.1 Neutrino event signatures

Two main types of neutrino event signatures can be distinguished by the IceCube detector, namely the track-like and the shower-like events². The track-like events are produced when muon neutrinos undergo a charged current interaction. This interaction yields a long-lived muon that can travel several tens of kilometres, leaving an elongated track in the detector [9]. The shower-like events are produced from the charged current interactions of the other neutrino flavors (electron and tau neutrino) as well as the neutral current interaction of all neutrino flavors. These interactions generate electromagnetic and hadronic showers that typically propagate less than 20 m with 90% of the light emitted within 4 m of the shower maximum [9]. Figure 3–5 shows simulations of the propagation of Cherenkov light in the Antarctic ice for both of the main neutrino event signatures. The angular resolution of track-like events is generally lower than $\sim 1^\circ$, while shower-like events have an average angular resolution of $\sim 15^\circ$. Consequently, track-like events are favoured targets for neutrino astronomy.

² A third signature, the so-called double-bang event, is expected for the interaction of the tau-neutrino when the tau track is longer than a few tens of meters. Two separate showers could then, in theory, be seen: the first at the vertex of interaction of the neutrino and the second at the tau decay vertex. No such double pulse events were found in the first 3 years of IceCube data. This result is consistent with the 0.54 expected events from simulations if cosmic neutrinos arrive at Earth with a flavor ratio of 1:1:1. [8]

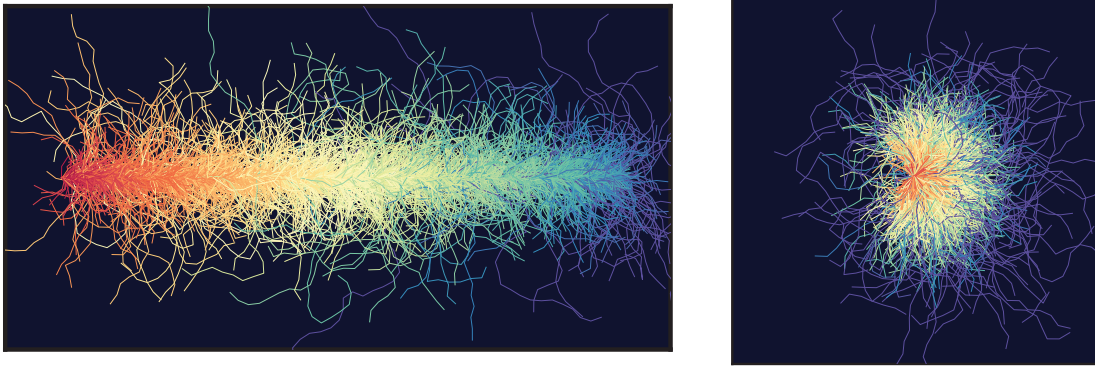


Figure 3–5: Simulated Cherenkov photons for the two main neutrino interactions in Antarctic ice. The figure on the left shows a simulated track-like event and the figure on the right shows a simulated shower-like event. Each track corresponds to the trajectory of a photon. Early photons are in red and late photons are in blue [8].

3.2.2 Starting events

”Starting events” are identified in IceCube as neutrinos for which the interaction vertex is located within the instrumented volume of the detector. This rejection strategy is sensitive to both track-like and shower-like events and therefore to every neutrino flavor. As mentioned previously, the outer layer of the detector can be used as a veto. Events are then rejected if a certain number of photons are detected in the veto region at an earlier time than the interaction vertex. 37 starting neutrino event candidates with deposited energy higher than 30 TeV were found from the analysis of the first three years of IceCube data, from 2010 to 2012. The properties of these events can be found in Supplementary Table I of [1]. Extending the data to four years, 17 new starting event candidates were found for a total of 54. The properties

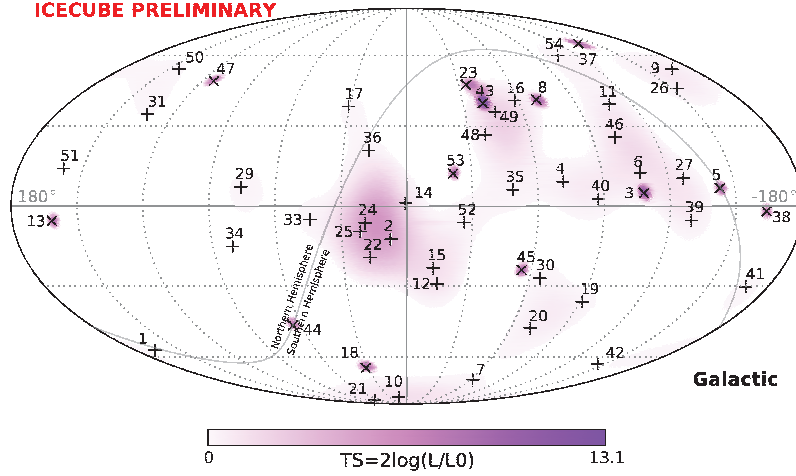


Figure 3–6: Arrival direction of the 54 “starting neutrino event” candidates found in four years of data. The + symbols mark the shower-like events and the × symbols mark the track-like events. The color denotes the test statistic (TS) for the point-source clustering test at each position. The square root of the TS approximately corresponds to the significance (σ). No significant clustering was found. Figure taken from [1].

of the events from the fourth year of data can be found in [4]. Figure 3–6 shows the arrival directions of the 54 starting events in galactic coordinates.

3.2.3 Through-going muons

Another strategy used by IceCube for the detection of astrophysical neutrinos is to restrain the analysis to muon tracks coming from below the detector. Those muons necessarily come from neutrino interactions, since no muon could go through the whole Earth diameter without being absorbed. This method does not require the neutrinos to interact inside IceCube’s volume and therefore, has the advantage of substantially increased effective area of the detector. However, this search is limited to Northern hemisphere sources only and is sensitive to cosmic neutrinos of energy above $E_\nu \sim 200$ TeV [8]. More than 35000 neutrinos were found from the analysis of

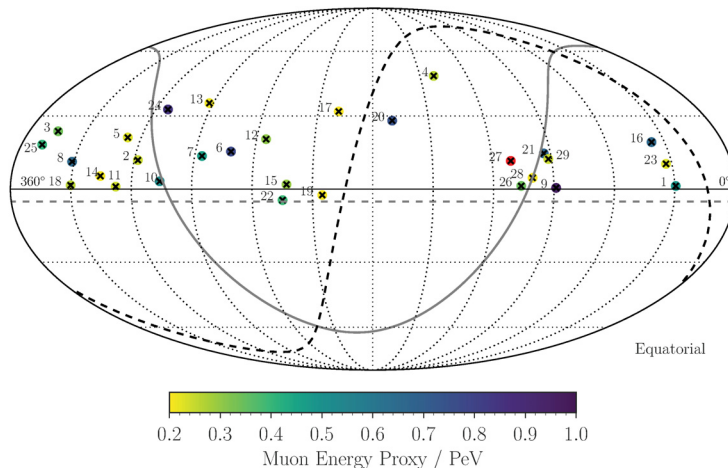


Figure 3–7: Equatorial skymap showing the arrival directions and energies of the 29 most energetic up-going muon track events with energy higher than 200 TeV published in [5]. Events ID 1 and 2 were also included in [2], events ID 3-16 in [3] and event 21 corresponds to the starting event ID 38 from [1].

the first two years of IceCube data, including 21 with an energy higher than 100 TeV. At this energy, the rate is inconsistent with neutrinos produced in the atmosphere and the analysis suggests that more than half of them are of cosmic origin [3,17]. The analysis was recently extended to 6 years, including data from May 2009 to April 2015 and a list of the highest energy events above 200 TeV was published in [5]. Figure 3–7 shows the location and energy of each of these 29 events projected on an equatorial map. Event ID 27 is so far the most energetic neutrino event registered by IceCube, with a deposited energy of 2.6 ± 0.3 PeV [5]. This PeV track-like event recorded by IceCube on June 11 2014 is displayed in figure 3–8.

3.3 Combined results

No significant point source of neutrinos was found in the analysis of 7 years of IceCube data [6]. Figure 3–9 shows a sky map of p-values representing the probability

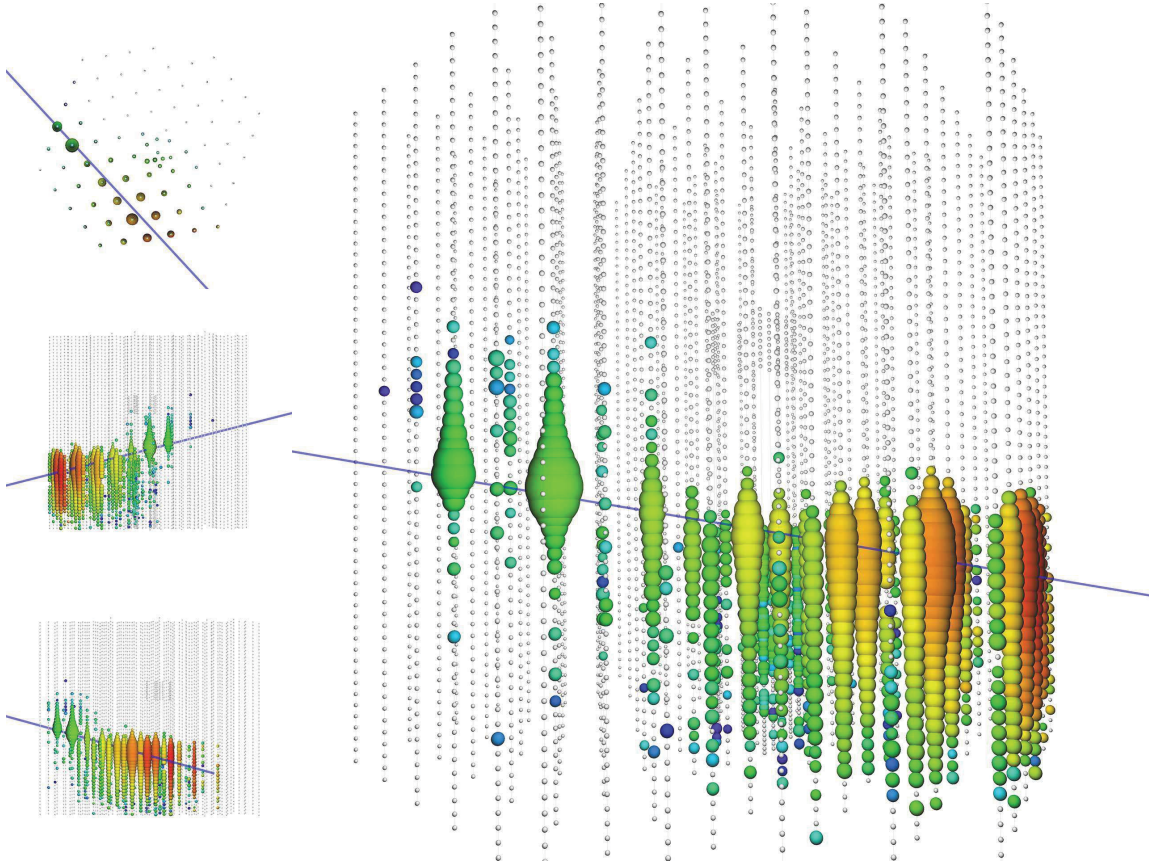


Figure 3–8: Event view of the PeV event muon track inside the detector. The top and two side views are shown on the left. The colors indicate the photon arrival times, red being early and green being late. The size of the sphere represents the measured charge in a logarithmic scaling. A double sphere size corresponds to a hundred times more charge [5].

that an excess of events is due to background fluctuations. Despite the absence of point sources, spectral analysis of the combined results has been made. It results in a spectrum from 27 TeV to 2 PeV, consistent with an unbroken power law. The best-fit power index is -2.49 ± 0.08 and the integral flux is $7.0_{-1.0}^{+1.0} \times 10^{-18} \text{ GeV}^{-1} \text{ s}^{-1} \text{ sr}^{-1} \text{ cm}^{-2}$ [4]. The analysis of muon tracks with an energy above 200 TeV in the 6-year IceCube data set resulted in a harder spectrum:

$$\Phi_{\nu+\bar{\nu}} = (0.90_{-0.27}^{+0.30}) \cdot (E_{\nu}/100 \text{ TeV})^{-(2.13 \pm 0.13)} \quad (3.1)$$

in units of $10^{-18} \text{ GeV}^{-1} \text{ s}^{-1} \text{ sr}^{-1} \text{ cm}^{-2}$ [5]. As pointed out in [8], this may indicate a spectrum hardening at high energy. The best-fit spectrum for the combined analysis is displayed in figure 3–10.

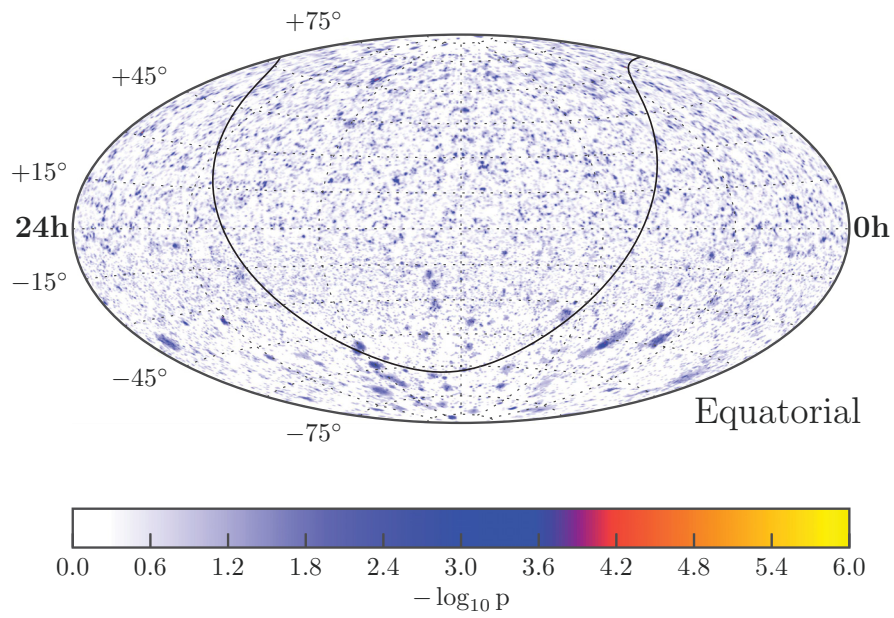


Figure 3–9: All-sky map of the negative logarithm of the pre-trial p-value assuming no clustering as the null-hypothesis. Taken from [6].

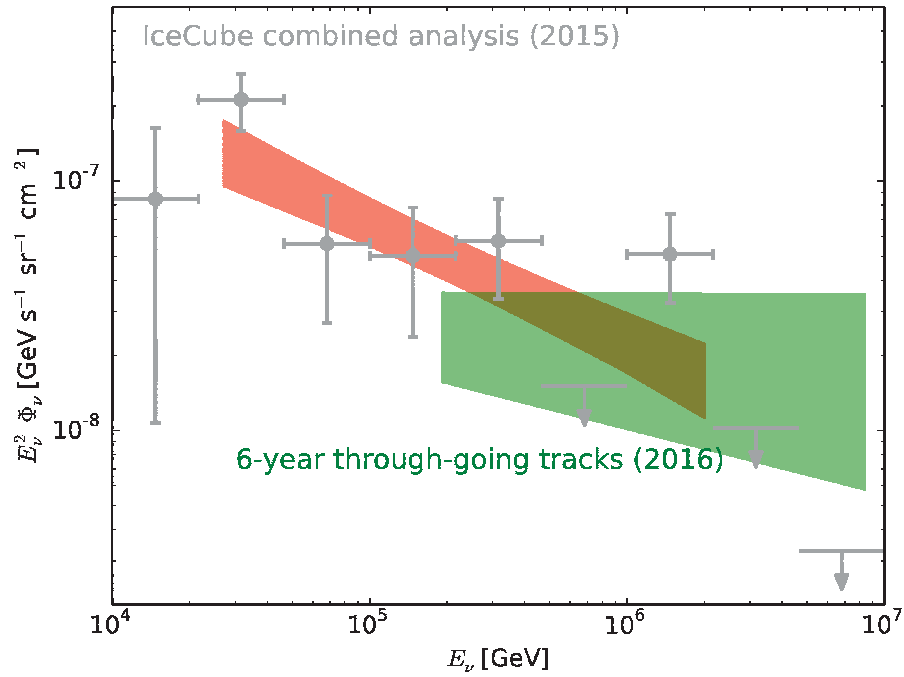


Figure 3–10: Spectrum of the combined analysis of extra-solar neutrino candidates found by IceCube. The red bar indicates the best fit to the data with a single power law spectrum hypothesis. The green bar shows the fit to the results of the through-going muon track analysis, having a harder spectrum index. From [8].

CHAPTER 4 VERITAS experiment

VERITAS is an acronym for Very Energetic Radiation Imaging Telescope Array System. It is a γ -ray observatory located near Tucson in southern Arizona, at 31.675° N, 110.952° W and at an altitude of 1268 m. It consists of four 12-meter Imaging Atmospheric Cherenkov Telescopes (IACTs). The telescopes have a field of view of 3.5° and the array is sensitive to an energy range of 85 GeV to 30 TeV, which is primarily in the very high energy (VHE, $E > 100$ GeV) range. The observatory's first light with the complete array was in April 2007. Two major improvements of the array were made in 2009 and 2012. The first consisted of the displacement of the first telescope, which improved the sensitivity. The second was the replacement of the photo-multiplier tubes from the cameras, improving the quantum efficiency. Figure 4–1 shows a photograph of the VERITAS array taken in 2009, after the displacement of the first telescope to its final position. The data used for the analysis presented in this thesis is only recent data for which the telescopes are in the final configuration with the upgraded PMTs.

4.1 Imaging Atmospheric Cherenkov Telescope

The technique used by IACTs consists of using the atmosphere as a particle detector. The interaction of cosmic-rays and γ -rays entering the atmosphere produces a cascade of relativistic particles. The passage of these secondary particles in the atmosphere causes the emission of Cherenkov radiation along the direction of the



Figure 4–1: The VERITAS array and buildings in September 2009. Photograph taken from [29].

shower. For primary energies ranging from 100 GeV to 1 TeV, the maximum emission is produced at an altitude of ~ 10 km, where the number of particles is the largest [33]. This results in a light pool of approximately 130-meter radius on the ground. The peak wavelength of the Cherenkov photons on the ground is $\lambda \approx 300\text{-}350$ nm and the density is approximately 100 photons/m² for a 1 TeV primary energy. These Cherenkov flashes last for only a few nanoseconds and can be detected by specially designed optical telescopes on the ground. Figure 4–2 shows a cartoon of the IACT technique.

4.1.1 History

The first mention of the atmospheric Cherenkov phenomenon is credited to the British physicist Patrick Blackett, who estimated in 1948 that 0.01% of the night-sky light must come from cosmic-ray-induced Cherenkov radiation [38]. Five years later, Bill Galbraith and John Jelley used a 25 cm parabolic mirror and a 5 cm diameter PMT housed in a garbage can to test this prediction. The PMT was

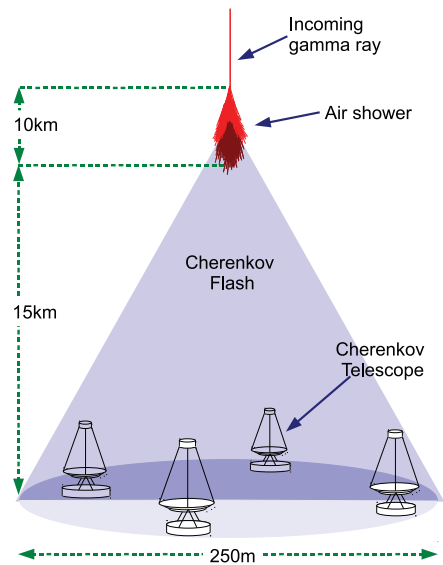


Figure 4–2: Depiction of the Cherenkov emission from an air shower and its detection on the ground by an IACT array. Figure taken from [29].

coupled to an amplifier whose output was displayed on a oscilloscope. Galbraith and Jelly observed an excess of light triggering over the background about once every two minutes. Subsequent experimentation showed that this excess was indeed Cherenkov radiation associated with extended air showers. The first attempts to detect γ -rays using this technique were made using ex-World War II searchlight mirrors and by looking for point-sources over the isotropic cosmic-ray background. The Whipple 10 m telescope, built in 1968 on Mount-Hopkins in Arizona, was the first purpose-built ground-based γ -ray telescope and is the direct predecessor to VERITAS. Despite their ability to detect γ -rays, the initial atmospheric Cherenkov telescopes had no way to discriminate the γ -rays from the much more numerous cosmic-rays. Therefore

no γ -ray sources were found until the detection of the Crab pulsar by the Whipple telescope in 1989.

4.1.2 Imaging Technique

The success of Whipple and the following modern IACTs (VERITAS, H.E.S.S. and MAGIC) lies in the differentiation of the image morphology between the cosmic-ray and the γ -ray induced showers. A γ -ray entering the atmosphere produces an electron-positron pair which then induce an electromagnetic cascade. Cosmic-rays entering the atmosphere induce a more complex cascade due to hadronic interactions. Secondary nucleons, along with charged and neutral pions are produced. The charged pions then decay into muons and neutrinos, while the neutral pions decay into γ -rays, which induce electromagnetic showers. As shown in figure 4-3, these types of showers differ considerably and the shape of the images in the telescope cameras can therefore be used to accomplish the γ /hadron separation. Modern IACTs can accomplish 99.999% of cosmic-ray rejection, while keeping up to 50% of the γ -ray events [33].

4.2 Instrument

The VERITAS telescopes are composed of an azimuth-elevation positioner, a 12-meter multi-segmented mirror and a camera box at its focal point. Each telescope is accompanied by a trailer in which the camera readout electronics and monitoring systems are stored. Figure 4-4 shows the fourth telescope with its different parts identified.

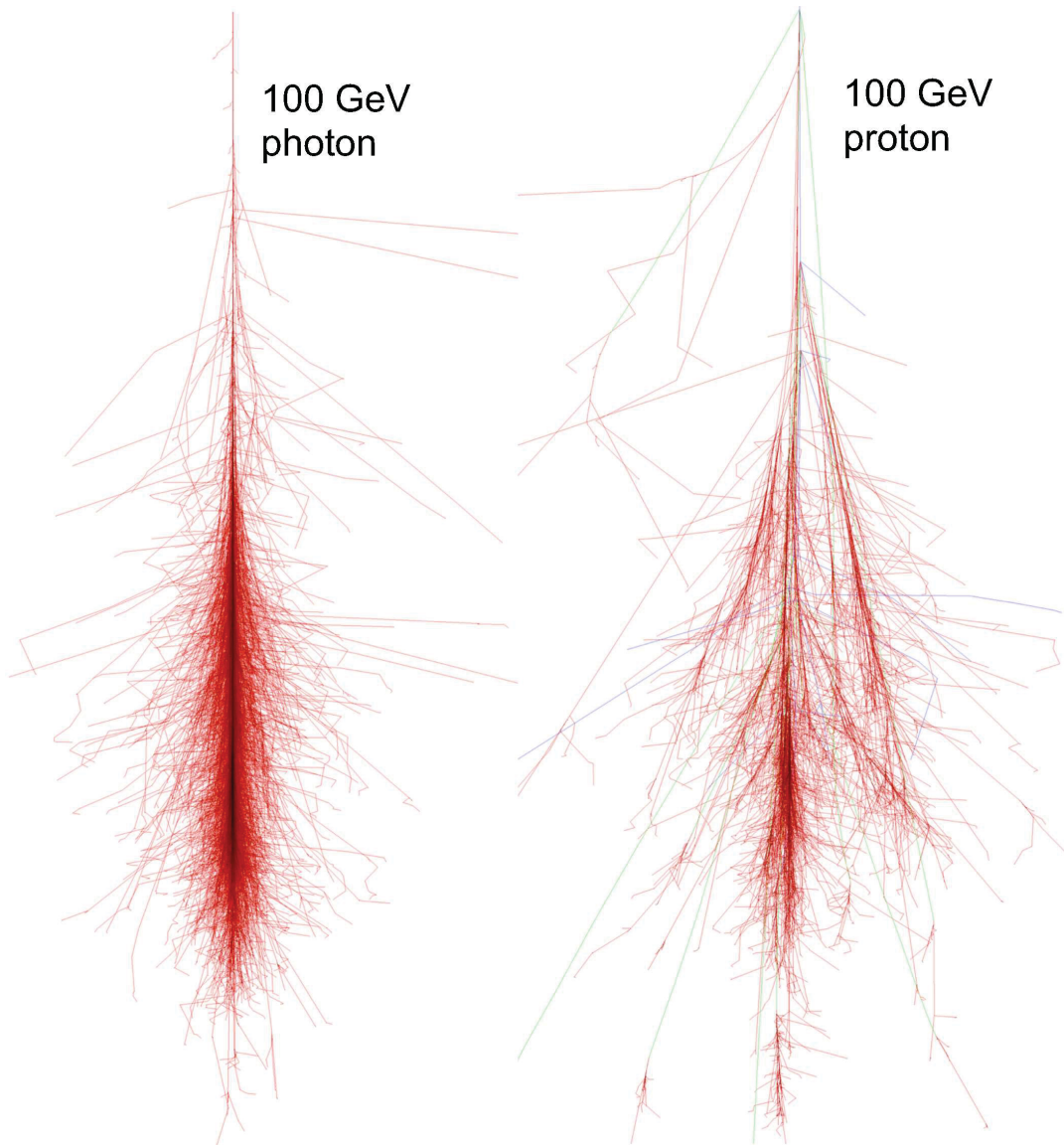


Figure 4-3: Monte Carlo simulations of the charged particle tracks in air showers caused by a 100 GeV photon and a 100 GeV proton entering the atmosphere. Figure taken from [25].

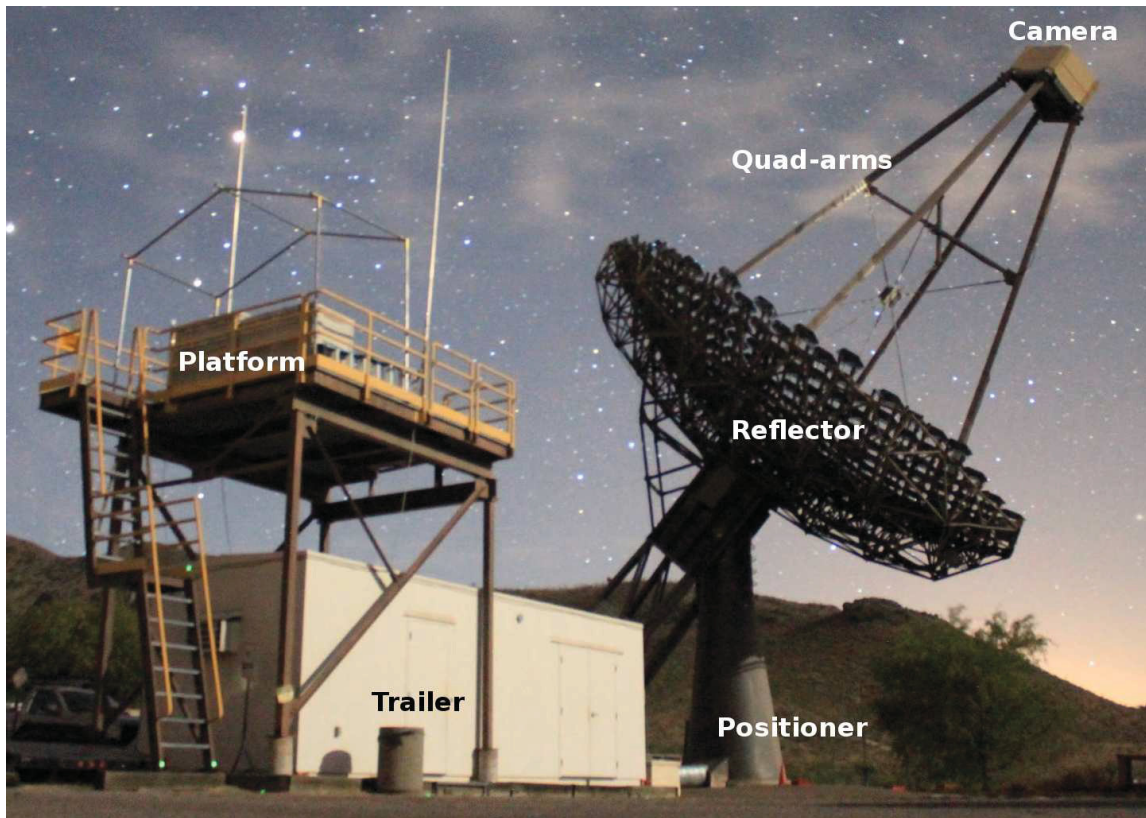


Figure 4-4: Photograph of Telescope 4 observing under moonlight with its different components indicated.

4.2.1 Telescopes

The pointing of VERITAS is ensured by an azimuth-elevation positioner. Its slewing speed is approximately $1^\circ/\text{s}$ and its pointing accuracy is 50-100 arcseconds. The use of a pointing monitor camera comparing the position of stars in the field of view with their actual coordinates reduces the pointing error to ~ 25 arcseconds. The optical reflectors of the VERITAS telescopes are a combination of 350 identical mirror facets based on the Davies-Cotton design [19]. This specific design allows to build larger reflectors at a lower cost. The mirror facets are 35cm-edge hexagons and have a curvature radius of 24 meters. They are mounted on a spherical optical support structure (OSS) of 12-m radius. Each mirror facet is fixed to the OSS using three mounting bolts, which can be adjusted for orientation.

4.2.2 Camera

At the focal point lies the camera, which is held by the quad-arms. It consists of 499 one-inch Hamamatsu R10560-100-20 photomultiplier tubes organized into an hexagonal configuration, totalling the 3.5° field of view. The left panel of figure 4–5 depicts the actual PMTs used by VERITAS along with the previous Photonis XP 2970 which were used before the 2012 upgrade. The R10560 has a peak quantum efficiency of $\sim 35\%$ at 350 nm and a charge collection efficiency of $\sim 90\%$ [22]. The quantum efficiency of the actual Hamamatsu and old Photonis PMTs as a function of wavelength is shown on figure 4–6. On the same graph is also shown the Cherenkov light at the ground from a simulated 500 GeV gamma ray entering the atmosphere. The Cherenkov spectrum has a cutoff at low wavelength due to the absorption of UV photons by ozone and Rayleigh scattering. In order to reject light that is not

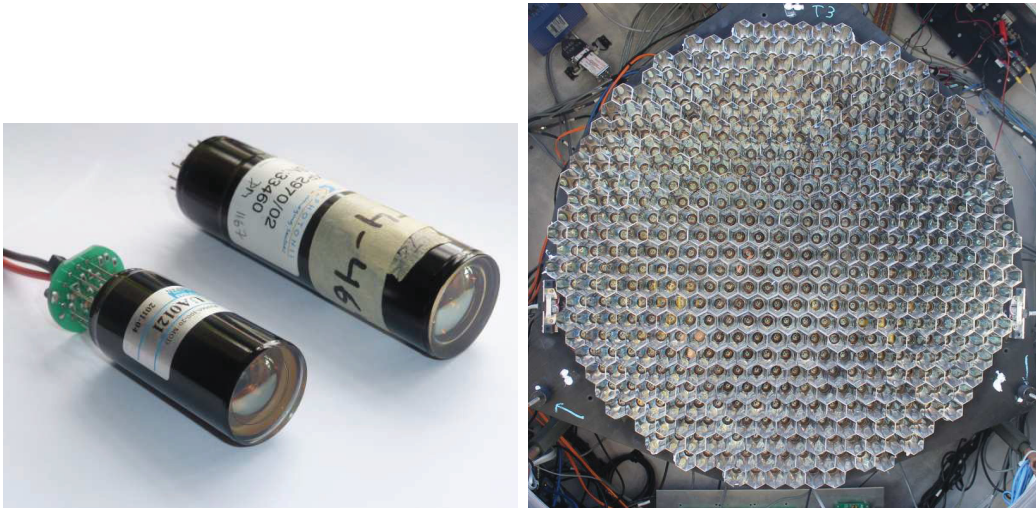


Figure 4–5: *Left:* Photograph of the Photonis XP 2970 PMT (right) used before 2012 and the Hamamatsu R10560-100-20 PMT (left) used after the 2012 array upgrade. Figure taken from [31]. *Right:* Picture of the camera with the light cones installed onto the PMTs.

coming directly from the reflector, light cones are installed in front of every PMT. The light cones are closely packed into hexagons, reducing the dead space between each pixel. The right panel of figure 4–5 shows a picture of the camera with the light cones installed on the PMTs. The PMTs are run at a gain of 2×10^5 , which means that for every photo-electron produced at the photo-cathode, 2×10^5 electrons reach the anode. This corresponds to a charge of $2 \times 10^5 \times q_e$ C \approx 0.03 pC. Each PMT is connected to a preamplifier which amplifies the signal by a factor of 6.6 before passing through the 45 m cable linking the PMTs to the electronics in the trailers. A remote-controlled shutter protects the phototubes from the sunlight during the day.

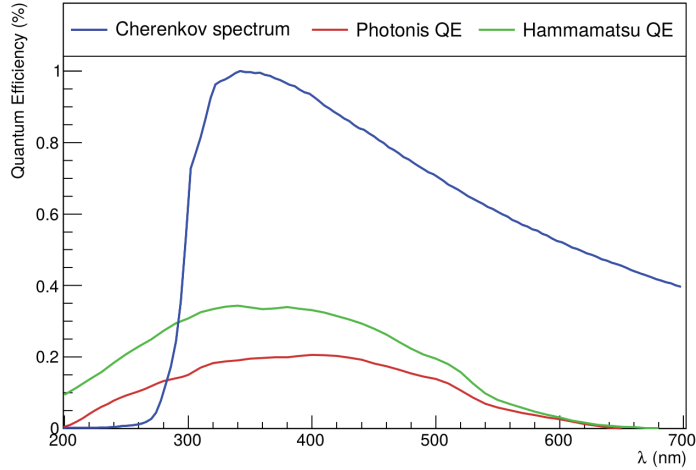


Figure 4–6: Quantum efficiency of the previous PMTs used by VERITAS, compared to the new ones as a function of the wavelength. Also shown is the simulated Cherenkov spectrum on the ground from a 500 GeV gamma ray entering the atmosphere. The Cherenkov spectrum shows a cutoff at low wavelength due to the absorption of UV photons by ozone and the Rayleigh scattering. Figure taken from [22].

4.2.3 Data acquisition

The signal from each PMT is continuously digitized by flash analog-to-digital converters (FADCs) and stored in a $65 \mu\text{s}$ ring buffer. Figure 4–7 shows an FADC trace produced by Cherenkov light from a cosmic ray air shower. Most of the PMT signals, however, don’t come from Cherenkov light, but rather from the night sky background (NSB), which causes $\sim a \text{ few } \times 10^{12} \text{ photons m}^{-2} \text{ s}^{-1} \text{ sr}^{-1}$ to fall on the ground [22]. In order to reject this overwhelming background and be more sensitive to the Cherenkov light from air showers, a three-level trigger system is used by VERITAS. The first level (L1) consists of a pixel-level trigger. It triggers based upon the number of photoelectrons hitting a PMT. This L1 trigger is very sensitive to noise and dependant on the NSB. Its rate is on the order of $\sim a \text{ few MHz}$. The

second level (L2) trigger is a pattern trigger. Taking the output of the L1, the L2 trigger looks for the coincidence of three neighbouring pixels within a 5-ns time window. The typical L2 trigger rate is ~ 4000 Hz. This trigger level cuts on the NSB background and keeps mostly Cherenkov events. The third and final level (L3) trigger is the array trigger. It triggers if any two telescopes have a L2 trigger within a 50-ns time window. This L3 trigger is good at reducing cosmic muons, which generally produce a ring of Cherenkov light on a single telescope. The L3 trigger has a typical rate of ~ 450 Hz. Once the trigger criteria is satisfied, the data is stored to disk. Every FADC trace is registered and packaged into an event. All events are then compressed and stored into a VERITAS bank format (VBF) file and ready for offline analysis. The typical length of a run is 30 minutes and the resulting file size is ~ 10 GB.

4.2.4 Calibration

The PMTs of the cameras are calibrated using LED flashing devices; the so-called "flashers". Each telescope is equipped with a flasher located on the cross bar of the quad-arms, 4 meters away from the camera. The flashers are modified torch lights containing 7 LEDs behind a diffuser which uniformly shines light at the PMTs alternating from 0 to 7 LEDs. Every observing night, a flasher run is taken, during which the PMTs are flashed and triggered at a typical rate of 300 Hz. The response of each PMT to the same amount of light is then compared to the average and the relative gain is adjusted for the analysis.

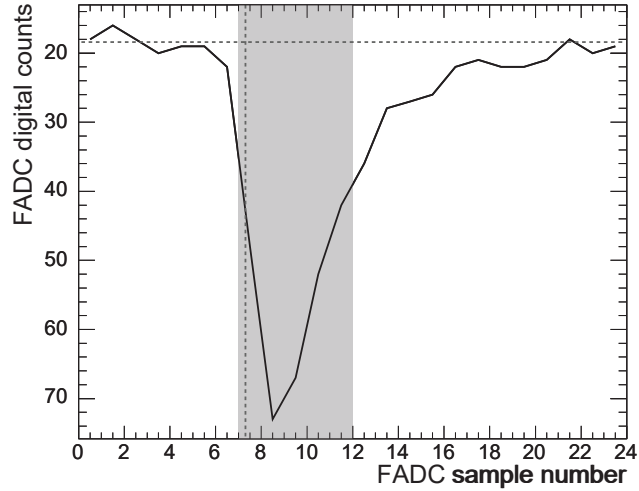


Figure 4–7: FADC trace produced by the Cherenkov light from a cosmic ray air shower as shown in a single channel. Each FADC sample corresponds to 2 ns. Figure taken from [26].

4.3 Analysis technique

The strategy used for the data analysis of IACTs consists of tracing back to the initial gamma ray which entered the atmosphere, starting from the signal detected by the telescopes. To do so, the morphology of the image is used to deduce the height and distance of the shower to the array. Having this in hand, the intensity of the Cherenkov light can be compared to simulation to determine the energy of the initial gamma ray. Two analysis packages are used by the collaboration: Eventdisplay and VEGAS (VERITAS Gamma-ray Analysis Suite). The packages have the same functionality and each analysis is generally verified by both packages. For the analysis presented in this thesis, the VEGAS package was used.

4.3.1 Image cleaning

The daily flasher run is first analyzed, from which the gain and timing information of each channel is extracted and used to flat-field and correct the timing of the camera. During each run, the telescopes are artificially triggered once per second in order to measure the pedestal, corresponding to the NSB light. The variance of the pedestal (pedvar) is proportional to the noise, therefore the pedvar is calculated and stored as a measurement of the noise. The first two panels of Figure 4–8 show a raw image of a shower before and after subtraction of the pedestal. This image is still very noisy and a cleaning method is used to isolate the signal from the shower. The first pass of the cleaning consists of looking for pixels that have a signal-to-noise ratio superior to 5, which means that the integrated charge for that pixel is at least 5 times larger than the pedvar. These pixels are tagged as picture pixels. The neighbouring pixels of the picture pixels are then examined. They are retained and tagged as boundary pixels if their signal to noise ratio is higher than 2.5. The third and fourth panels of Figure 4–8 shows the image after the cleaning was applied. Finally if a picture pixel has no neighbouring image pixel, it is removed, as shown on the last panel of Figure 4–8.

4.3.2 Parameterization

Now that the images have been cleaned, they can be characterized using the method developed by A. M. Hillas [23]. The method consists mainly of approximating the image as an ellipse and calculating its parameters. Figure 4–9 shows the different Hillas parameters of an image. Among the Hillas parameters, the ones still in use in stereoscopic arrays are described in Table 4–1. A first quality cut is then made based

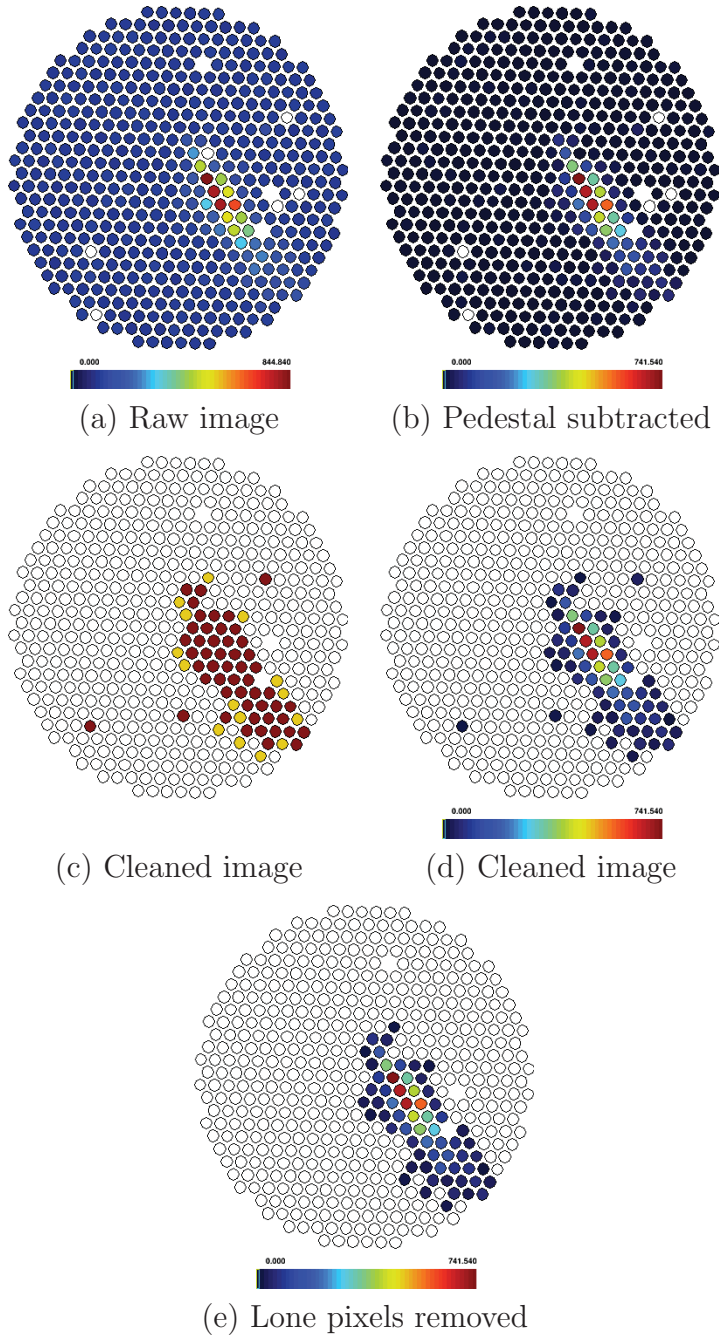


Figure 4-8: Different steps of the image cleaning method. The colour scheme represents the charge measured by each pixel, in dc, except in (c) for which maroon represents picture pixels and gold represents neighbouring pixels. This image was obtained from simulating the detector response of T2 to a 800 GeV photon entering the atmosphere.

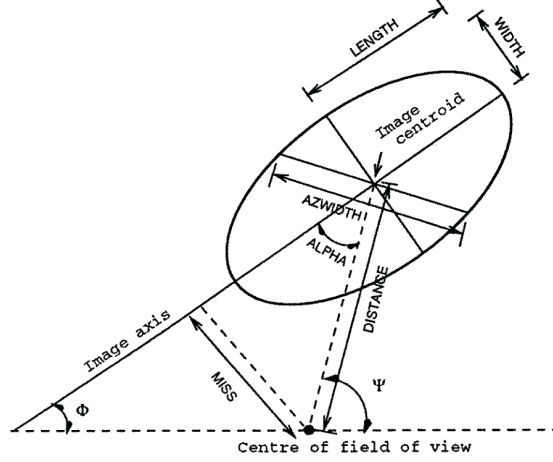


Figure 4–9: Main Hillas parameters for a single telescope. Figure taken from [20].

on these parameters to remove images that would be problematic to reconstruct. The standard quality cut values used by VEGAS are shown in the second column of Table 4–1. VERITAS being a stereoscopic array, an additional quality cut is made, requiring more than one telescope with an image of the shower.

4.3.3 Event reconstruction

Once the quality cuts have been applied, the images taken by different telescopes can be used in a combined analysis to reconstruct the event. The air shower follows the orientation of the particle that initiated it. Since the shower occurs at an altitude of ~ 10 km, the image will appear differently in every telescope. Figure 4–10 shows the same image of the air shower created by a simulated 800 GeV gamma-ray as seen by all four telescopes. The arrival direction of the initial gamma-ray can be determined by projecting all four images of the shower on the camera plane, as shown on the left panel of Figure 4–11. The best-fit location of the intersection point of the major axes pinpoints the direction. Alternatively, by projecting the

Table 4–1: The main Hillas parameters for a single telescope that are still in use in stereoscopic arrays. The second column shows the regular values of the quality cuts applied by VEGAS. The *Size* cut value varies as a function of the analysis. The values shown here are for the soft cuts analysis, used for this thesis.

Hillas parameter	Value	Description
Size	>400 dc	Sum of the charge of all the channels that passed the image cleaning cut
nTubes	>5	Number of phototubes in the image
Distance	<1.43°	Distance in degrees between the centre of the field-of-view and the image centroid
Width	-	The spread of light along the minor axis
Length	-	The spread of light along the major axis

different images on the ground, at the location of the telescopes, the position of the shower on the ground can be determined. This is shown on the left panel of Figure 4–11. The distance between the shower on the ground and the centre of the array is known as the impact parameter. Additional parameterization can be done taking into account the multiple images. The θ^2 parameter corresponds to the square of the angular distance between the reconstructed position of the event in the camera and the assumed location of the source. The *MeanScaledWidth* (*MeanScaledLength*) corresponds to the average ratio of the width (length) of the ellipse and the width (length) of the image of a simulated gamma-ray shower, taking into consideration the telescope pointing, impact parameter and shower size. The expression of the *MeanScaledWidth* (MSW) parameter is as follows:

$$MSW = \frac{1}{N_{images}} \left[\sum_i^{N_{images}} \frac{width_i}{w_{MC}(R, s, \Theta)} \right] \quad (4.1)$$

Table 4–2: Summary: VEGAS regular soft cuts for nominal (reduced) HV.

Cut name	Value	
	Lower Cut	Upper Cut
Mean scaled width	0.05	1.1
Mean scaled length	0.50	1.3
θ^2 [deg ²]	–	0.03 (0.01)
Maximum shower height [km]	7	–

where w_{MC} is the width from Monte Carlo simulations, as a function of R , the impact parameter, s , the image size and Θ , the telescope pointing. The summation is conducted over every telescope containing an image. The simulations used are conducted multiple times and take into account the atmosphere, NSB, telescope optics, etc. to be as close as possible to a real shower. The results of the simulations are stored in lookup tables, which also contain the energy of the shower.

4.3.4 Gamma/hadron separation

To select gamma-ray events and reject the extremely more numerous background cosmic-ray events, a set of cuts on the stereo parameters is applied. Since the MSW and MSL are expected to have a value of one for gamma-ray events, events with a large value of these parameters are rejected. Cuts are also applied on events that have a θ^2 that exceeds a certain value. Another parameter known as the *MaxHeight* corresponds to the height of the peak emission of the shower. It can be determined using the centroids of the shower images, the impact and source location and the energy of the shower recovered from the simulation tables. Cuts are also applied on this *MaxHeight* parameter. Table 4–2 shows a summary of the regular VEGAS soft cuts that were used for this analysis.

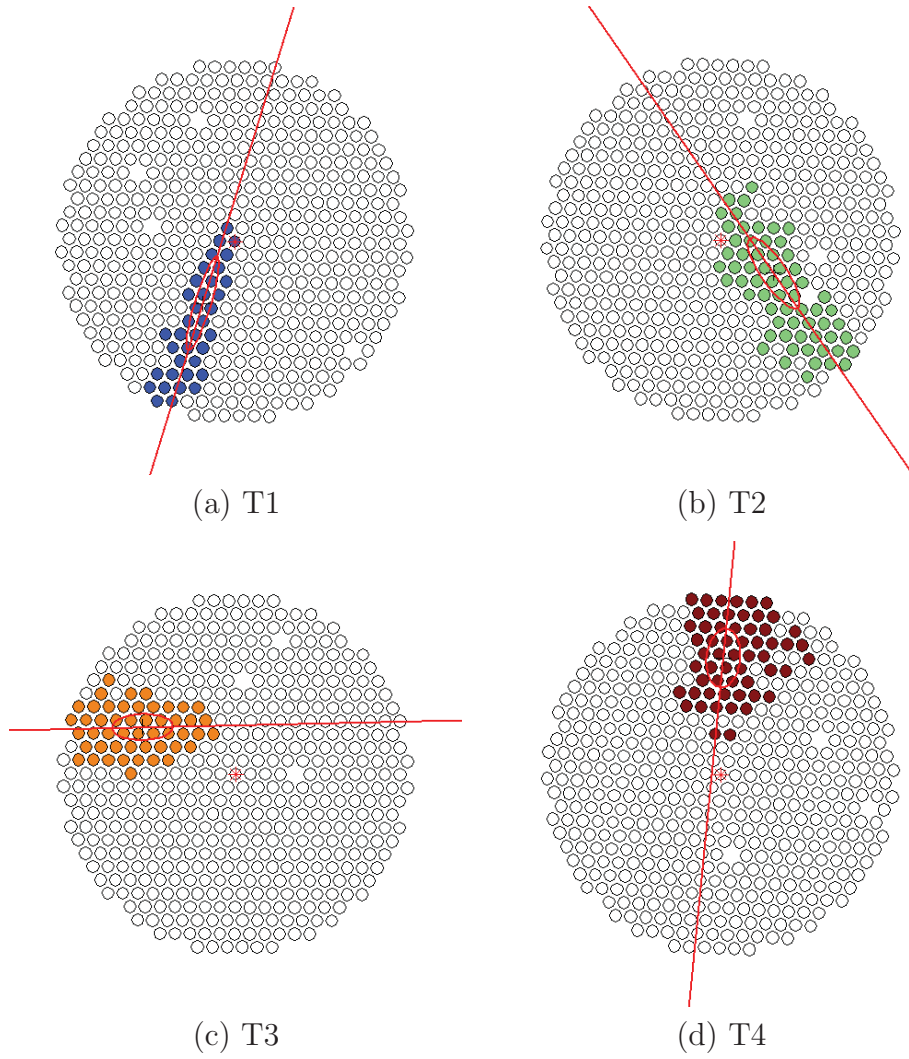


Figure 4-10: A simulated gamma-ray shower, as seen by the telescopes after image cleaning. Due to the low altitude of the shower and the spacing of the telescopes, the images differ between the telescopes.

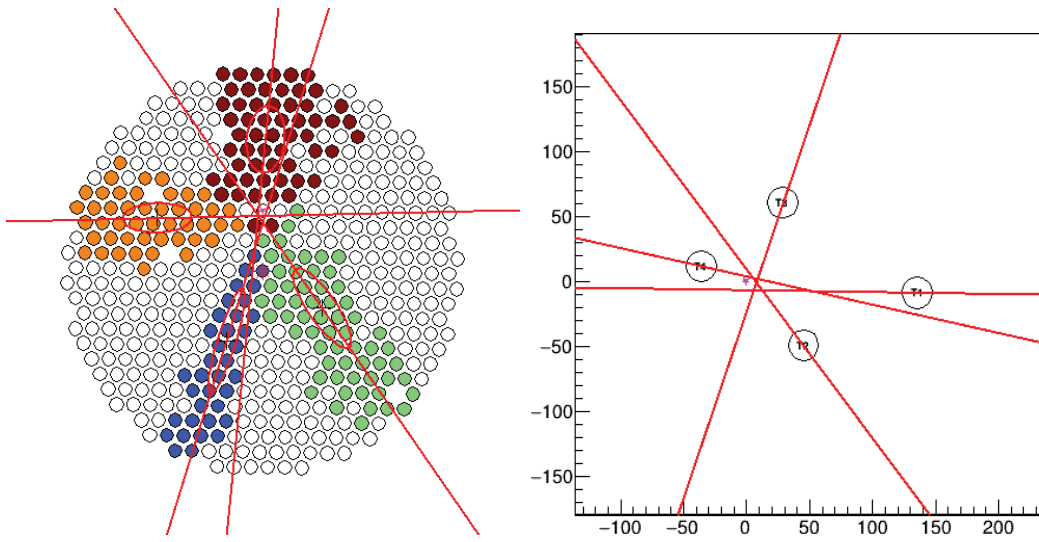


Figure 4–11: *Left:* All four images taken by the telescopes projected onto the camera plane. The best fit to the intersection of the ellipses' major axes pinpoints the arrival direction of the gamma-ray in the sky. *Right:* By projecting the images on the ground, the best fit to the intersection of the ellipses' major axes corresponds to the ground location of the gamma-ray shower.

4.3.5 Significance and skymap

Different methods are used to estimate the number of gamma-ray like events coming from the source and from background. The method used for the analysis presented in this thesis is the reflected region method. It consists of observing with a 0.5° offset (can be 0.7° or 1.0° depending on the source) and alternating between each cardinal direction for each run. This is referred to as wobble observation mode. A source region is then defined with a certain radius as well as background regions with the same radius and situated at the same distance from the centre of the camera, as seen in Figure 4–12. The number of events is then counted in the source region (N_{on}) and in the background region (N_{off}). The number of excess events is simply

$$N_{excess} = N_{on} - \alpha N_{off} \quad (4.2)$$

where α is the ratio of the acceptance of the *on* region to the acceptance of the *off* region. The acceptance is the likelihood that a signal is to be measured and varies with the radial distance from the centre of the camera. For the reflected region technique, since the *on* and *off* regions are of the same size and at the same radial distance from the centre, α is simply the inverse of the number of *off* regions ($\alpha = 1/(\text{number of off regions})$). Knowing N_{on} , N_{off} and α , the significance can be calculated using equation 17 from [27]:

$$S = \sqrt{2} \left\{ N_{on} \ln \left[\frac{1 + \alpha}{\alpha} \left(\frac{N_{on}}{N_{on} + N_{off}} \right) \right] + N_{off} \ln \left[(1 + \alpha) \left(\frac{N_{off}}{N_{on} + N_{off}} \right) \right] \right\}^{1/2} \quad (4.3)$$

By calculating the significance at each point in the field of view, a significance skymap can be obtained. A histogram of the significances in each bin can also be made, known

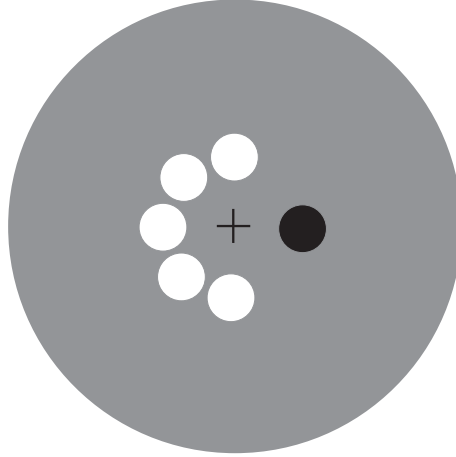


Figure 4–12: Illustration of the wobble observation mode as well as the reflected region technique. The black circle represents the source region, the white circles represent the background regions and the black cross is the centre of the field of view.

as a significance distribution. In the absence of a source the significance distribution should be a Gaussian centred at zero with a standard deviation of 1. Figures 4–13 and 4–14 show respectively the significance map and significance distributions of the analysis of ~ 80 minutes of data on the Crab nebula.

4.3.6 Flux and upper limit

The rate of gamma-rays detected by the array is simply

$$R_\gamma = \frac{N_{on} - \alpha N_{off}}{\tau} \quad (4.4)$$

where τ is the livetime of the array, that is the kept observation time corrected by the deadtime. In order to calculate the flux, the effective area of the detector must be known. This is a complicated matter since it depends on many different factors, including the NSB, the atmospheric conditions, the pointing, etc. Similarly to the

Significance Map (smoothed)

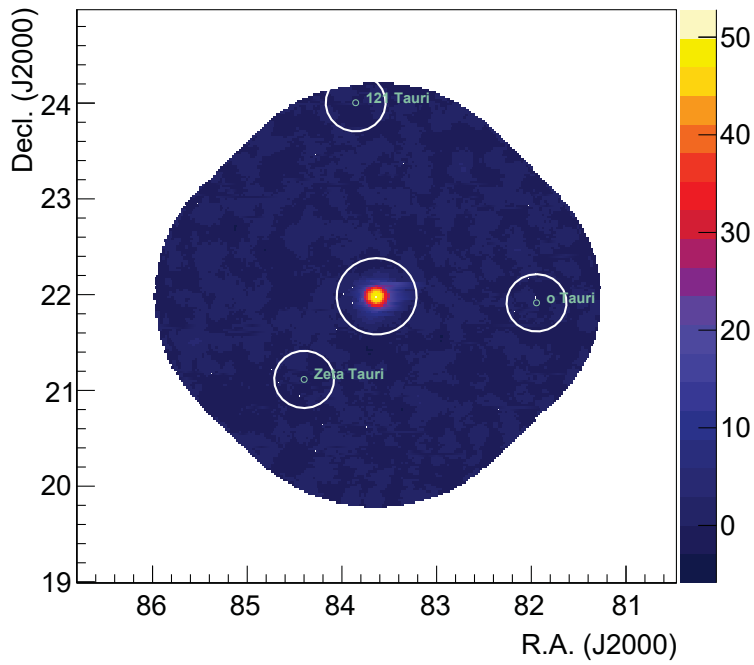


Figure 4–13: Skymap of the Crab nebula as obtained by VEGAS analysis of approximately 80 minutes exposure time data. The circle at the centre corresponds to the source region and the other circles are excluded regions due to the presence of bright stars in the FOV. The significance of the detection here exceeds 50σ .

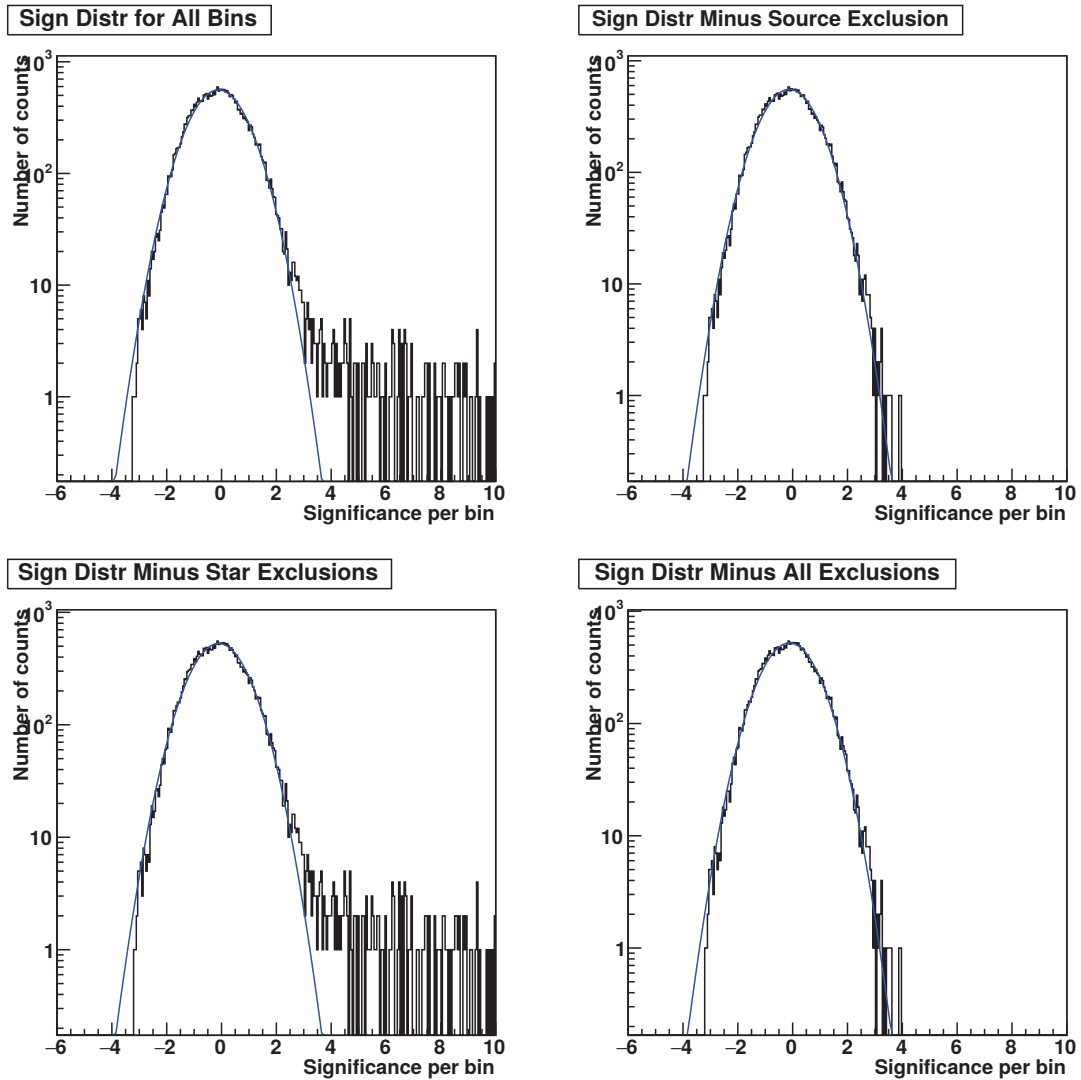


Figure 4-14: Significance distributions for the same Crab nebula data analysis shown in figure 4-13.

parameterization of MSW and MSL, simulations are used to calculate the effective area. In the case where there is not a significant detection reached, an upper limit on the flux can be calculated. To do so, an upper limit on the number of excess events is compared to the number of expected events from an input spectrum. The method used in this thesis is the Rolke method [35].

CHAPTER 5

VHE gamma ray counterparts to IceCube neutrinos

5.1 Event selection

From all the neutrino candidate events recorded by IceCube, only the ones coming from the northern hemisphere can be followed up by VERITAS. The first criteria for VERITAS to accomplish a follow-up observation on an IceCube event are therefore the coordinates of its arrival direction. Also, since the shower-like events have a poor angular resolution (see Section 3.2), only the track-like events will be followed up by VERITAS. The higher the energy of the reconstructed neutrino, the greater is its probability of being astrophysical and the better is its angular resolution. As a result, VERITAS followed up the most energetic neutrino events as a priority.

In total, VERITAS collected several dozens of hours of data coming from 28 different IceCube event locations. Out of these 28 neutrino events, 4 correspond to starting events, here labelled as ICECUBE_ID, and 24 correspond to through-going muon events, here labelled as IC_NU. Since the majority of the IceCube event follow-up observations started before the IceCube collaboration published them, the ID numbers differ. Also, the reconstructed arrival directions slightly differ from one publication to the other while VERITAS collected data from the same location that was initially communicated by IceCube. Some variations in the location of the neutrino events are then present and were taken into account for this analysis.

Table 5–1: IceCube high-energy starting event (HESE) positions compared with VERITAS pointing.

VERITAS			IceCube 3-year and 4-year data [1, 4]				IceCube 6-year (2-year) data [5] ([3] ¹)							
ID	RA (°)	Dec (°)	ID	RA (°)	Dec (°)	Resolution (°)	ID	RA (°)	50% C.L.	90% C.L.	Dec (°)	50% C.L.	90% C.L.	Separation (°)
ICECUBE_ID5	110.6	-0.4	ID5	110.6	-0.4	$\lesssim 1.2$	(12)	(110.5)	-	-	(0)	-	-	(0.41)
ICECUBE_ID13	67.9	40.3	ID13	67.9	40.3	$\lesssim 1.2$	-	-	-	-	-	-	-	-
ICECUBE_ID37	167.3	20.7	ID37	167.3	20.7	$\lesssim 1.2$	-	-	-	-	-	-	-	-
ICECUBE_ID38	93.3	14.0	ID38	93.3	14.0	$\lesssim 1.2$	21	93.38	+0.33 -0.34	+0.83 -0.90	14.48	+0.40 -0.39	+0.86 -0.94	0.50

Table 5–2: IceCube through-going muon event positions from 2-year and 6-year data compared with VERITAS pointing

VERITAS			IceCube 2-year data [3] ¹				IceCube 6-year data [5]							
ID	RA (°)	Dec (°)	ID	RA (°)	Dec (°)	Separation (°)	ID	RA (°)	50% C.L.	90% C.L.	Dec (°)	50% C.L.	90% C.L.	Separation (°)
IC_NU2	88.6	0.2	2	88.5	0.2	0.14	9	89.0	+0.18 -0.25	+0.48 -0.53	0.5	+0.10 -0.10	+0.25 -0.21	0.42
IC_NU3	37.2	18.7	3	37.1	18.6	0.13	16	36.7	+0.61 -0.56	+1.85 -1.71	19.1	+0.54 -0.77	+2.21 -2.21	0.69
IC_NU4	346.9	24.1	6	346.8	24.0	0.14	3	344.9	+1.14 -1.04	+2.90 -3.39	23.6	+0.91 -1.18	+2.31 -4.13	1.90
IC_NU5	331.1	11.1	5	331.0	11.0	0.12	8	331.1	+0.18 -0.35	+0.49 -0.80	11.1	+0.18 -0.19	+0.41 -0.49	0.02
IC_NU6	267.6	13.8	7	267.5	13.8	0.10	7	266.3	+0.22 -0.23	+0.58 -0.62	13.4	+0.24 -0.15	+0.52 -0.45	1.34
IC_NU7	238.4	18.9	8	238.3	18.9	0.13	-	-	-	-	-	-	-	-
IC_NU8	235.4	19.3	9	235.2	19.3	0.16	12	235.1	+0.89 -0.55	+2.70 -1.76	20.3	+0.44 -0.62	+1.00 -1.43	1.03
IC_NU9	323.5	2.8	11	323.3	2.8	0.15	-	-	-	-	-	-	-	-
IC_NU10	9.6	7.9	13	9.4	7.8	0.21	-	-	-	-	-	-	-	-
IC_NU11	207.4	6.7	14	207.2	6.7	0.17	-	-	-	-	-	-	-	-
IC_NU12	152.4	6.8	15	152.2	6.8	0.15	-	-	-	-	-	-	-	-
IC_NU15	139.0	47.6	20	138.9	47.6	0.09	4	141.3	+0.23 -0.16	+0.46 -0.45	47.8	+0.25 -0.22	+0.56 -0.48	1.51
IC_NU16	222.0	3.2	-	-	-	-	15	222.9	+0.90 -1.14	+1.95 -1.73	1.9	+0.57 -0.37	+1.25 -1.18	1.56
IC_NU17	31.4	11.9	21	31.2	11.8	0.18	23	32.9	+0.20 -0.27	+0.63 -0.62	10.2	+0.15 -0.15	+0.34 -0.49	2.27
IC_NU19 ²	181.8	38.6	-	-	-	-	-	-	-	-	-	-	-	-
IC_NU20	110.3	11.5	-	-	-	-	27	110.6	+0.16 -0.28	+0.46 -0.55	11.4	+0.07 -0.08	+0.17 -0.17	0.29
IC_NU22	170.1	27.7	-	-	-	-	20	169.6	+0.45 -0.48	+1.16 -1.11	28.0	+0.31 -0.23	+0.67 -0.66	0.49
IC_NU23	348.7	18.2	-	-	-	-	25	349.4	+1.13 -1.75	+2.89 -4.12	18.1	+0.75 -0.63	+1.94 -1.80	0.70
IC_NU24	224.6	-4.3	-	-	-	-	22	224.9	+0.33 -0.32	+0.87 -1.19	-4.4	+0.42 -0.39	+1.21 -0.94	0.27
IC_NU25	106.3	1.3	-	-	-	-	26	106.3	+0.86 -0.74	+2.27 -1.90	1.3	+0.33 -0.29	+0.83 -0.74	0.03
IC_NU27	32.9	10.3	-	-	-	-	23	32.9	+0.20 -0.27	+0.63 -0.62	10.2	+0.15 -0.15	+0.34 -0.49	0.07
IC_NU28	100.2	4.6	-	-	-	-	28	100.5	+0.23 -0.34	+0.95 -1.87	4.6	+0.19 -0.12	+0.68 -0.50	0.27
IC_NU29	205.2	-2.4	-	-	-	-	19	205.1	+0.17 -0.24	+0.54 -0.66	-2.4	+0.18 -0.19	+0.42 -0.51	0.10
IC_NU30	192.8	31.8	-	-	-	-	17	198.7	+0.49 -0.18	+1.44 -1.09	32.0	+0.30 -0.37	+0.81 -0.85	5.03

¹ The 2-year data events were not explicitly published in [3], but can be found on the IceCube collaboration website at : http://icecube.wisc.edu/icecube/static/science/HE_NuMu_data-table.pdf. Their ID numbers found in this table correspond to their rank in the table found on the IceCube website.

² IC_NU19 was never published by IceCube because it has an energy inferior to the threshold required for publication. Its coordinates were still sent to VERITAS, which did follow-up observations.

Tables 5–1 and 5–2 display the list of IceCube neutrino starting events and through-going muon events respectively that were followed up by VERITAS. It also contains the different corresponding ID numbers and the differences between the VERITAS pointing location and the reconstructed neutrino event arrival directions as published by IceCube. The event IC_NU19 was followed by VERITAS, but was never published since its energy happened to be under the threshold energy required by IceCube for publication. Consequently, this particular event doesn't have any updated position.

5.2 Observation summary

About half of the data was taken under moonlight conditions and therefore at reduced high voltage (RHV). During moonlight conditions, the PMTs are operated at reduced high voltage in order to limit the PMT currents to a safe level. This also reduces the trigger rate that would be overwhelmed by the NSB. In addition, it increases the energy threshold. To allow a larger field of view, around 60% of the data was taken at a large offset wobble of 0.7° instead of the 0.5° regular offset. Each configuration requires a specific set of instrument response functions (IRFs)³ that were chosen accordingly. In the scope of this thesis, the large offset RHV data was removed since the IRFs for such a configuration were not yet available. This reduces

³ The instrument response functions include simulations used for the mean scaled width parameterization, energy reconstruction and effective area calculation. See Section 4.3.

the amount of data available for analysis by approximately 40% and the number of IceCube sources goes down from 28 to 22.

As described in Section 4.2.3, VERITAS records data in VBF files, with each file containing a 30-minute run. For this work, a total of 91 runs taken between November 2013 and April 2016 were analyzed. Some of the runs were flagged by the data quality monitoring (DQM) because of observation issues such as weather and needed time cuts which were applied. Table 5–3 shows all the IceCube events observed by VERITAS along with the exposure time in each configuration after the quality cuts were applied.

5.3 Significance

The regular soft cut analysis described in Section 4.3 was carried out on all of the data. While an excess of bins with a significance $>3\sigma$ is particularly suggestive, an excess of $>5\sigma$ is what is generally accepted as necessary to claim a detection. Resulting in a maximum significance of 1.7σ , the point source analyses done at the centre position of the VERITAS pointing showed no significant excesses. In the case where the reconstructed event position was updated by subsequent IceCube publications, the point source analysis was repeated in this other location. No significant excesses were found in these second positions either, the highest significance being 1.6σ . Figure 5–1 shows the significance map and the significance distribution resulting from the analysis of VERITAS data coming from the direction of IceCube’s PeV event described in Section 3.2.3. This event is particularly interesting since it has the best angular resolution and the highest probability of being an astrophysical neutrino at 99.5% [5]. On the sky map are indicated the VERITAS pointing location

Table 5–3: List of IceCube high energy events observed by VERITAS with the observation time, in minutes, on each source. The observation times are broken down into each different combination of high voltage and wobble offset configuration. In the scope of this thesis, the Reduced HV 0.7° wobble offset were removed from the analysis. This corresponds to slightly more than a third of the whole data, but resulted in the complete removal of events IC_NU23, IC_NU24, IC_NU25, IC_NU27, IC_NU29 and IC_NU30, here shaded.

ID	Nominal HV		Reduced HV		Total
	0.5°	0.7°	0.5°	0.7°	
ICECUBE.ID5	25	161	0	0	186
ICECUBE.ID13	101	97	181	0	379
ICECUBE.ID37	72	59	85	58	273
ICECUBE.ID38	24	55	0	55	134
IC_NUC2	0	22	0	0	22
IC_NUC3	151	0	0	0	151
IC_NUC4	96	0	0	0	96
IC_NUC5	51	0	0	0	51
IC_NUC6	0	22	0	0	22
IC_NUC7	0	17	14	0	31
IC_NUC8	0	27	29	28	85
IC_NUC9	36	0	0	0	36
IC_NUC10	0	0	86	0	86
IC_NUC11	0	69	0	96	165
IC_NUC12	0	0	0	57	57
IC_NUC15	15	38	0	140	193
IC_NUC16	0	0	9	0	9
IC_NUC17	54	0	83	0	137
IC_NUC19	52	28	0	113	193
IC_NUC20	22	74	0	0	95
IC_NUC22	0	43	0	0	43
IC_NUC23	0	0	0	105	105
IC_NUC24	0	0	0	71	71
IC_NUC25	0	0	19	93	111
IC_NUC27	0	0	0	165	165
IC_NUC28	0	71	5	37	113
IC_NUC29	0	0	0	133	133
IC_NUC30	0	0	0	57	57
Total	698	782	512	1208	3200

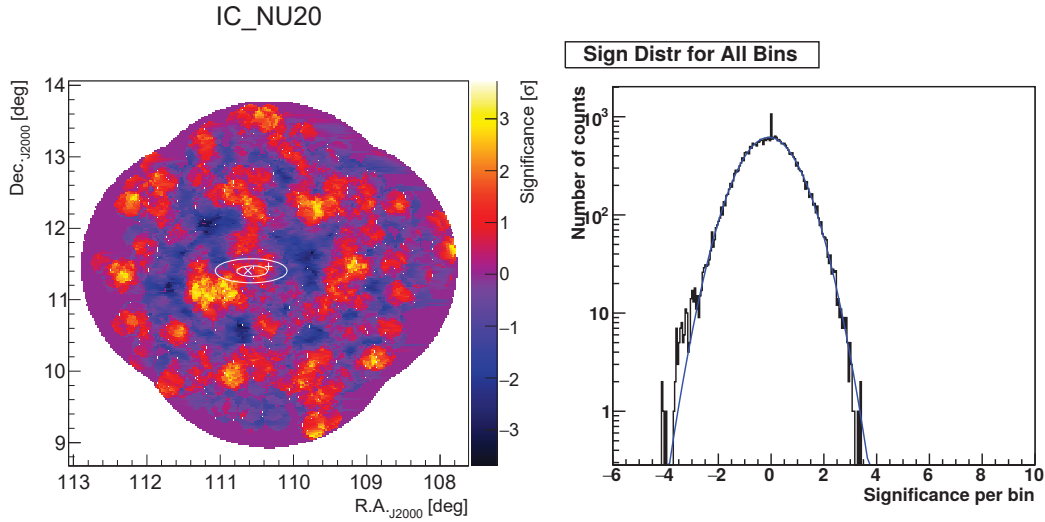


Figure 5–1: Significance map (left) and significance distribution (right) of the IceCube event IC_NU20, which corresponds to the event ID 27 as published in [5]. This is the PeV event described in Section 3.2.3. The “+” sign corresponds to the pointing position of VERITAS, while the “×” sign represents the position updated by IceCube in their most recent publication. The curves corresponds to the 50% and 90% confidence levels of the updated position.

and IceCube’s most recent update on the reconstructed event position along with the 50% and 90% confidence level curves. The significance maps and distributions of all the event follow-ups can be found in Appendix A. No significant hot spot can be found in any of the sky maps. Table 5–4 contains the values of the calculated significances at the VERITAS pointing positions and IceCube updated positions when applicable. The highest significance is of 1.7σ and was obtained at the centre maps of the three sources ICECUBE.ID37, IC_NU5 and IC_NU11. This significance level is statistically expected to occur 10% of the time and therefore, it is not significant.

5.4 Upper limit

Since no signals were detected, the calculation of upper limits (UL) on the flux have been done. As mentioned in Section 4.3.6, the UL was obtained using the Rolke method and was calculated at the 99% confidence level. The integral gamma-ray flux UL for every IceCube neutrino event can be found in Table 5–4. Again, the calculation was made at the centre position of the VERITAS pointing, as well as at the most recent IceCube reconstructed event position, when applicable.

The flux UL was also calculated in different energy bins in order to produce an UL spectrum. The four energy bins [126; 200], [200; 316], [316; 501] and [501; 794] GeV were used for each source. These bins were chosen as they are close to VERITAS energy threshold for these exposure times and soft cut analysis. This is therefore the region of the spectrum where the highest flux is expected. The 95% confidence level differential UL were calculated at the geometric centre of each bin, namely 158, 251, 398 and 631 GeV. Spectra of upper limits were made only for the VERITAS pointing positions. The flux UL spectrum of the IC_NU20 event is shown in Figure 5–2. The spectra for all other neutrino events can be found in Appendix B. Some spectra only have three or two bins, due to differences in the energy thresholds. The 1% and 10% flux from the Crab nebula were plotted on the same figures as a reference. As can be seen, most of the upper limits on the IceCube events lie somewhere around 10% Crab. This result shows that no VHE gamma-ray sources having a flux of 10% Crab or more were observed by VERITAS in the regions where IceCube detected high energy neutrino events.

Table 5–4: Summary of the results from the point source analysis of the IceCube events follow-up data observed by VERITAS, after subtraction of the Reduced HV large wobble offset data as mentioned in the text.

ID	Total exposure time [min]	VERITAS pointing position		IceCube updated position	
		Significance [σ]	Flux UL [$\times 10^{-8} \text{m}^{-2} \text{s}^{-1}$]	Significance [σ]	Flux UL [$\times 10^{-8} \text{m}^{-2} \text{s}^{-1}$]
ICECUBE_ID5	186	0.6	2.57	-	-
ICECUBE_ID13	379	0.9	4.28	-	-
ICECUBE_ID37	215	1.7	3.87	-	-
ICECUBE_ID38	78	1.0	4.92	0.9	7.87
IC_NUC2	22	-0.6	5.87	0.2	7.83
IC_NUC3	151	-0.6	1.57	0.4	2.84
IC_NUC4	96	1.1	4.02	-0.9	1.17
IC_NUC5	51	1.7	5.86	1.6	5.7
IC_NUC6	22	-2.6	0.01	-1.1	22.0
IC_NUC7	31	-1.3	2.74	-	-
IC_NUC8	56	-2.4	0.71	0.6	7.43
IC_NUC9	36	-0.1	4.81	-	-
IC_NUC10	86	-1.6	1.81	-	-
IC_NUC11	69	1.7	5.53	-	-
IC_NUC15	53	0.7	6.92	1.0	9.79
IC_NUC16	9	0.2	9.77	0.0	8.38
IC_NUC17	137	0.7	4.86	-0.3	1.59
IC_NUC19	80	1.6	6.16	-	-
IC_NUC20	95	0.2	2.22	0.4	5.75
IC_NUC22	43	-1.5	1.79	-1.3	18.2
IC_NUC25	19	0.3	9.80	0.1	8.87
IC_NUC28	76	0.4	3.17	-0.4	3.97

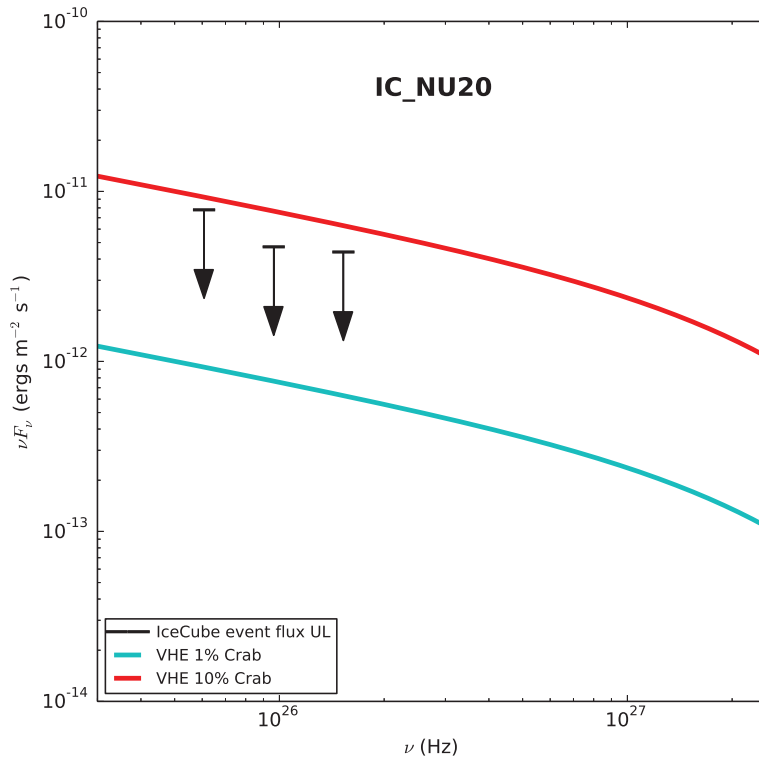


Figure 5–2: Spectrum of gamma-ray flux upper limits coming from the direction of the IceCube PeV neutrino event IC_NU20. The turquoise and red lines correspond respectively to 1% and 10% of the Crab nebula gamma-ray flux. As can be seen in this particular case, the flux UL lies between 1% and 10% the Crab.

CHAPTER 6

Conclusion

6.1 Summary

Within this thesis, the results of the efforts done by VERITAS to find a gamma-ray counterpart to IceCube high-energy neutrino events were presented. IceCube announced the first detection of a flux of astrophysical neutrinos in 2013 from the analysis of 2 years of data. The VERITAS multimessenger program was created shortly after, in order to search for gamma-ray sources in the regions corresponding to the arrival directions of some of the most energetic IceCube neutrino events in the Northern hemisphere. For this work, the analysis of the data of 22 different neutrino event follow-ups taken between November 2013 and April 2016 has been done. After some quality cuts, this corresponds to a total of ~ 33 hours of data.

No significant excess were found from the point source analysis done at the centre position of the skymaps, nor at the most recent positions updated by IceCube. No hot spots were found in any of the significance maps either. Gamma-ray flux upper limits were then calculated, constraining the flux of gamma-ray sources in the direction of IceCube neutrino events to be less than $\sim 10\%$ Crab.

6.2 Discussion

The absence of a gamma-ray counterpart found by VERITAS can be explained in different ways. As covered in Chapter 2, while gamma-ray sources do not necessarily emit neutrinos, the processes emitting neutrinos are expected to also produce gamma

rays. However, it is possible that these neutrino sources were so far away that gamma rays were partially absorbed on their way to the Earth. Perhaps, the gamma-ray fluxes were then too low to be detected (lying below the $\sim 10\%$ Crab upper limit calculated here).

Another possible explanation could be that the IceCube neutrino events were transient in nature and their gamma emission ceased long before VERITAS started its follow-up observations. Since none of the IceCube events share the same arrival directions, there is no evidence of a constant source of neutrinos. The hypothesis of the transient nature of the neutrino events is then valid.

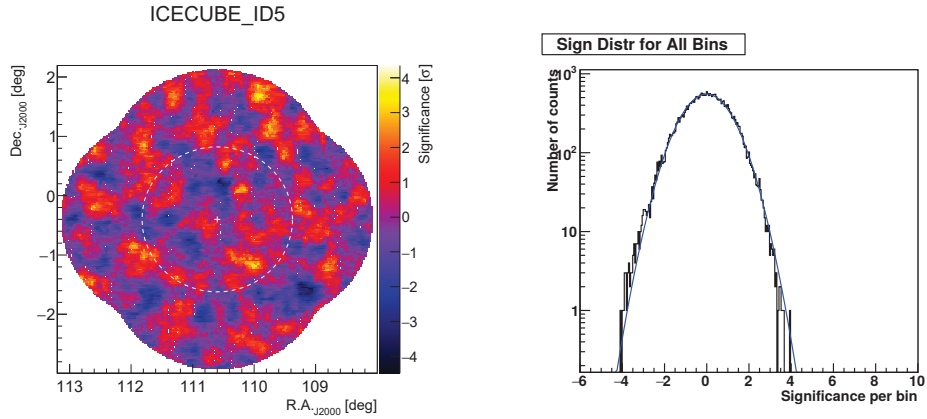
6.3 Future work

With more data, it would be possible for VERITAS to find gamma-ray sources that perhaps were too dim to be found with the actual data set. It could as well constrain the flux to a lower upper limit. Since the signal to noise ratio increases as the square root of the total observing time, doubling the amount of data would result in upper limits 1.4 times lower. On the other hand, the future generation of ground-based gamma-ray telescopes, such as the Cherenkov Telescope Array (CTA) [14], will have an improved sensitivity which will allow better performance for follow-up observations.

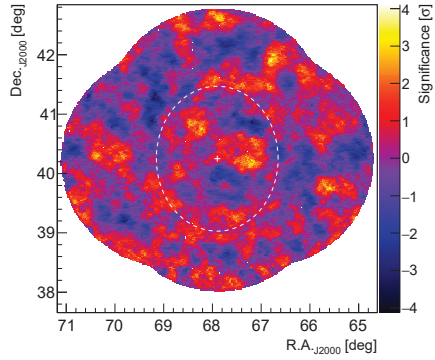
APPENDIX A

Significance maps and distribution

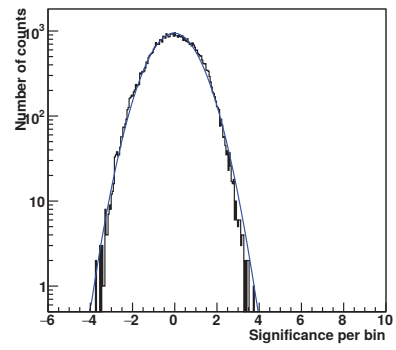
Following are the significance maps and significance distributions resulting from the analysis of VERITAS data coming from the different neutrino event positions. The “+” sign corresponds to the pointing position of VERITAS, while the “×” sign represents the updated reconstructed position by IceCube in their most recent publication. The solid-line curves correspond to the 50% and 90% confidence level of the updated position. For the HESE events that had no updated position, the region corresponding to the 1.2° resolution is shown as the dashed-line curves. No statistically significance excess was found for any of the events.



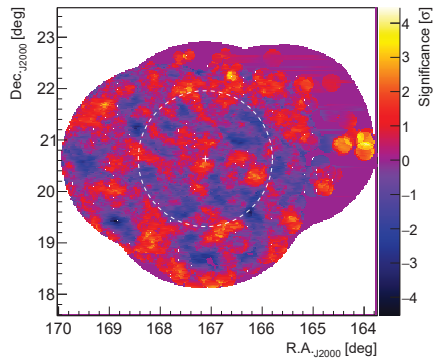
ICECUBE_ID13



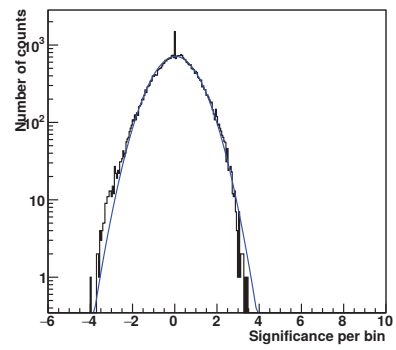
Sign Distr for All Bins



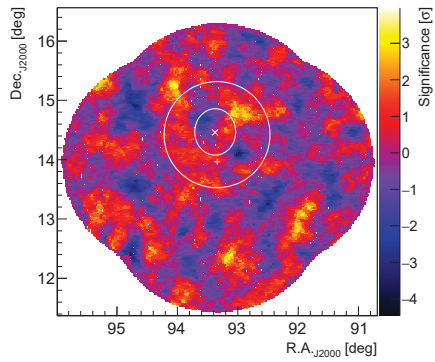
ICECUBE_ID37



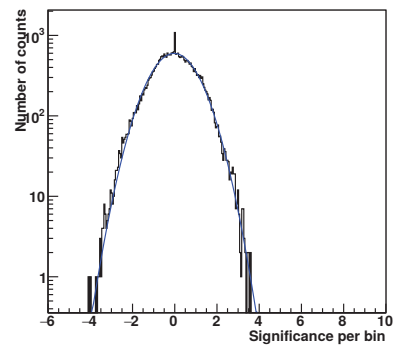
Sign Distr for All Bins



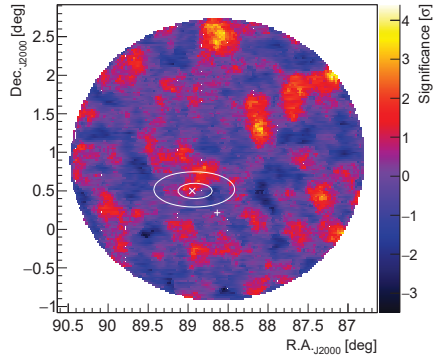
ICECUBE_ID38



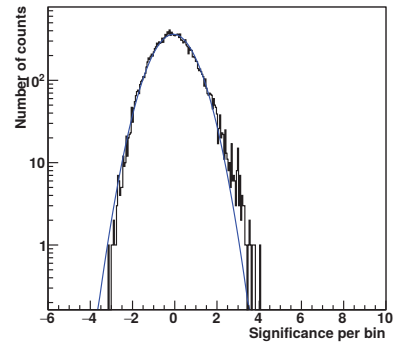
Sign Distr for All Bins



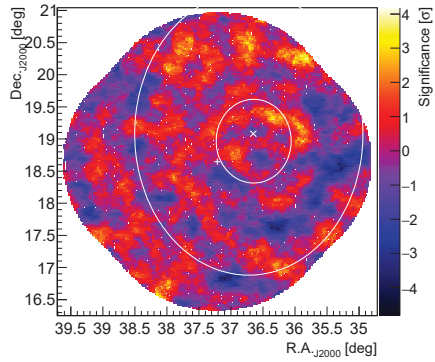
IC_NU2



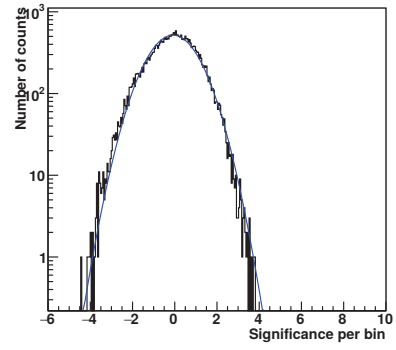
Sign Distr for All Bins



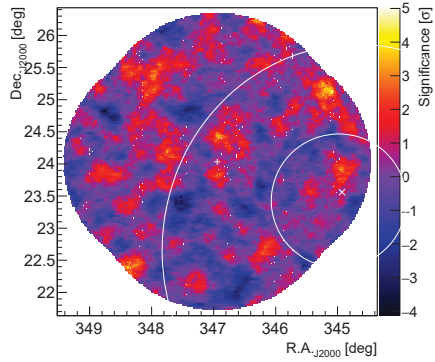
IC_NU3



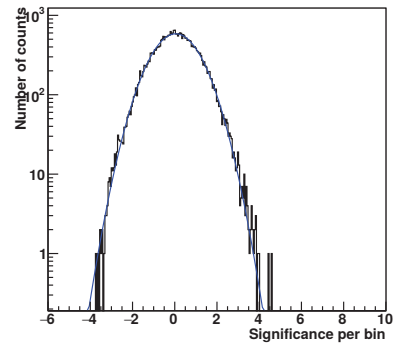
Sign Distr for All Bins



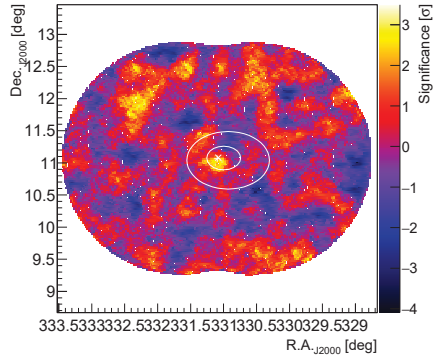
IC_NU4



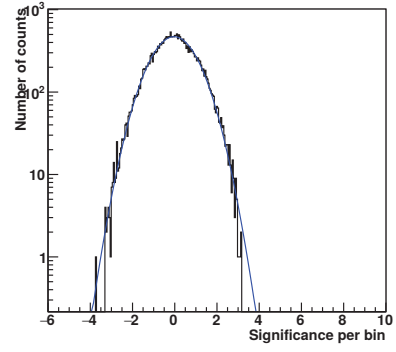
Sign Distr for All Bins



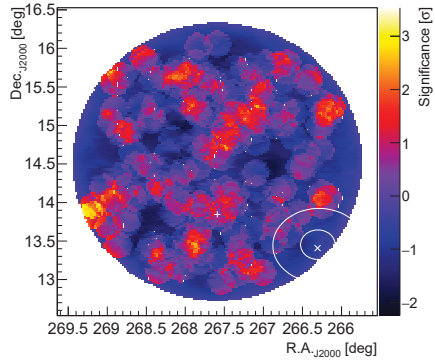
IC_NU5



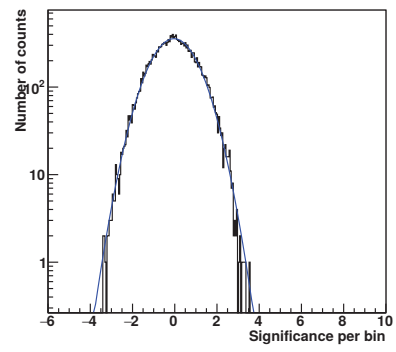
Sign Distr for All Bins



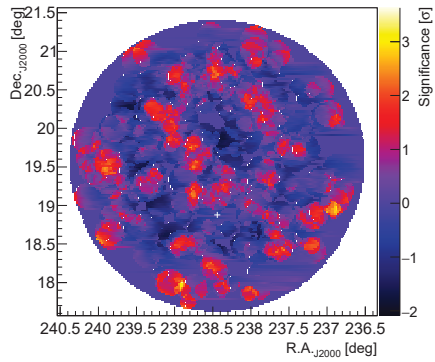
IC_NU6



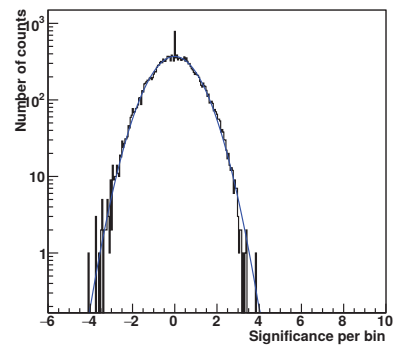
Sign Distr for All Bins



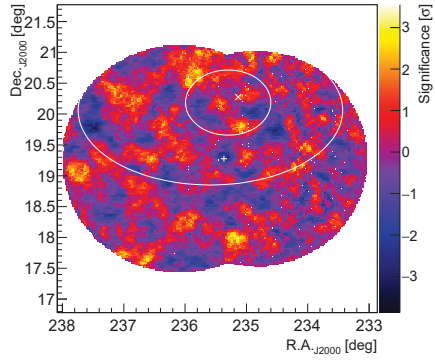
IC_NU7



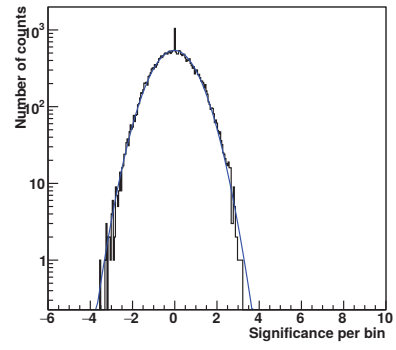
Sign Distr for All Bins



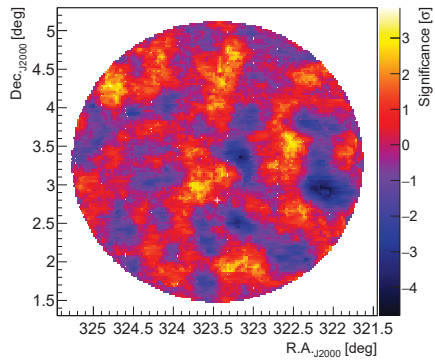
IC_NU8



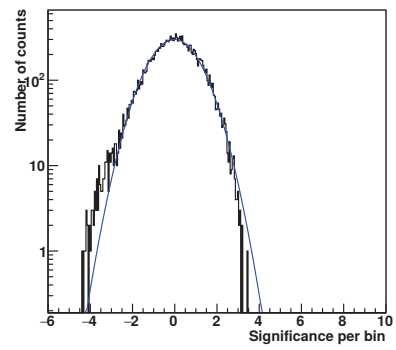
Sign Distr for All Bins



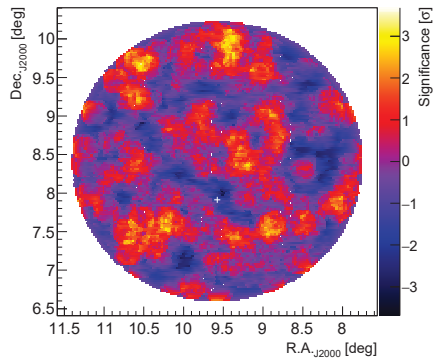
IC_NU9



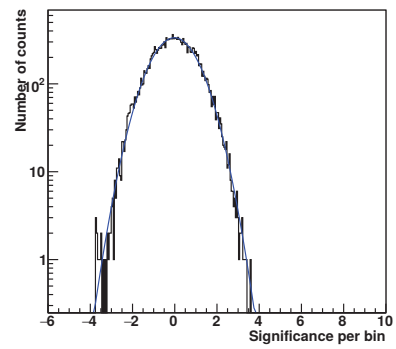
Sign Distr for All Bins



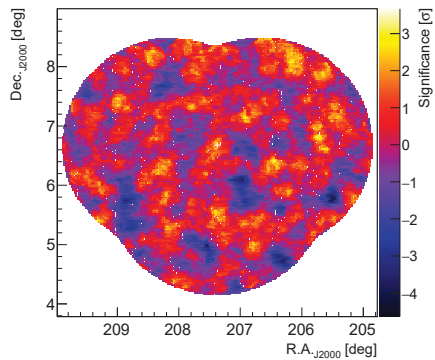
IC_NU10



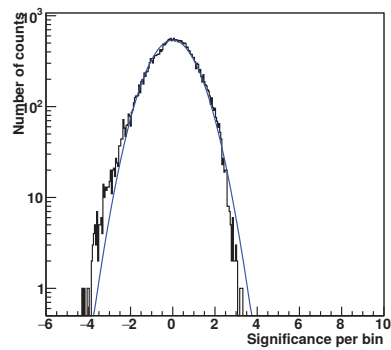
Sign Distr for All Bins



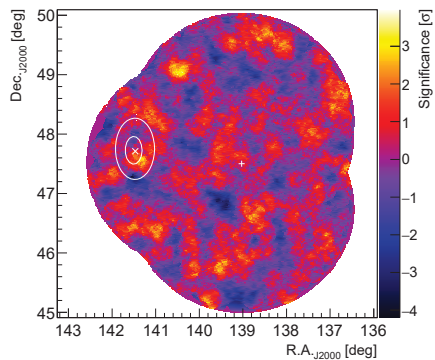
IC_NU11



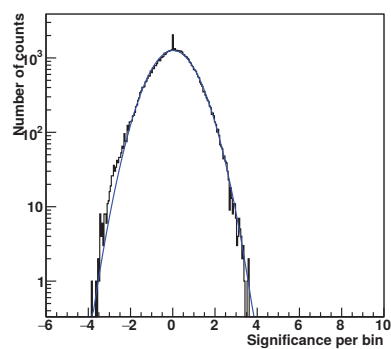
Sign Distr for All Bins



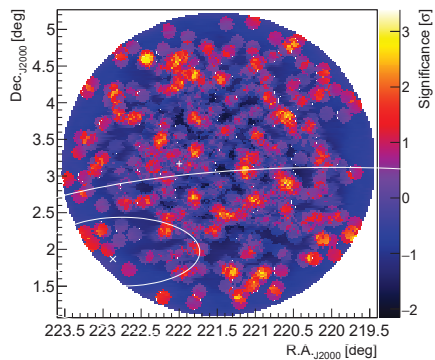
IC_NU15



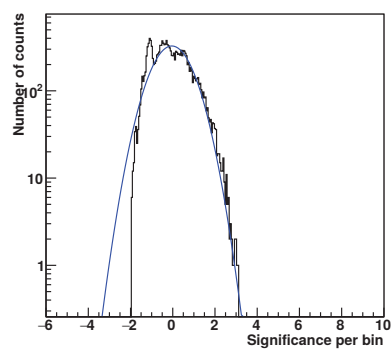
Sign Distr for All Bins



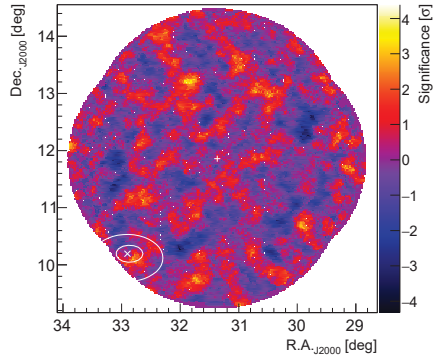
IC_NU16



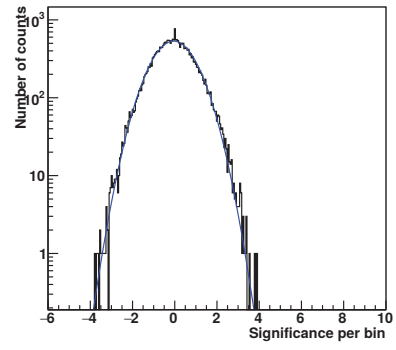
Sign Distr for All Bins



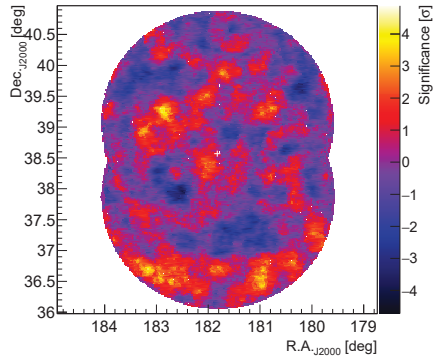
IC_NU17



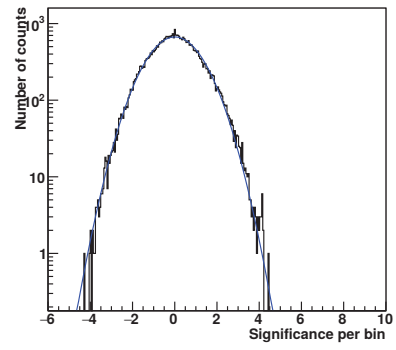
Sign Distr for All Bins



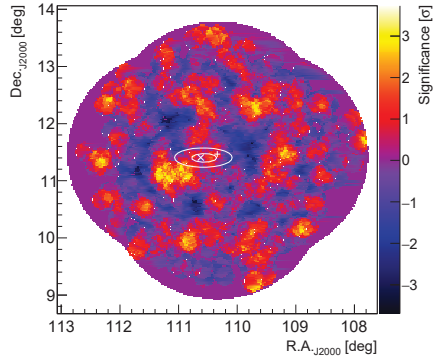
IC_NU19



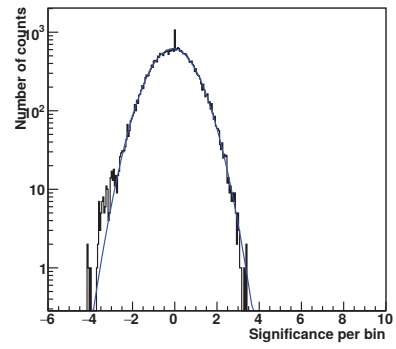
Sign Distr for All Bins



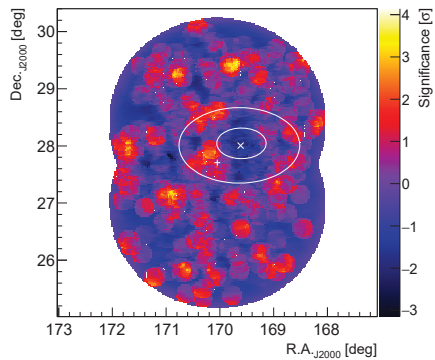
IC_NU20



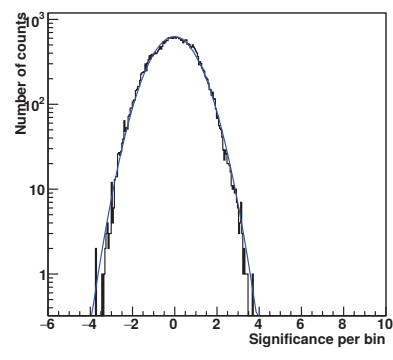
Sign Distr for All Bins



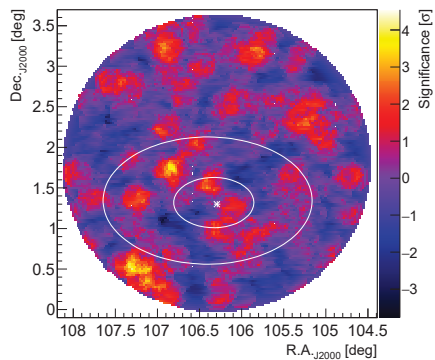
IC_NU22



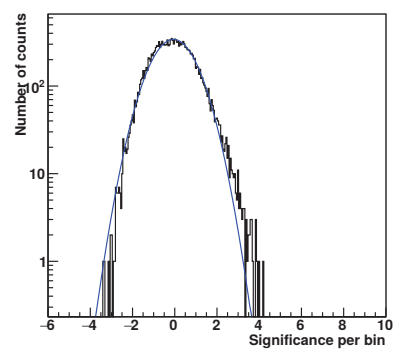
Sign Distr for All Bins



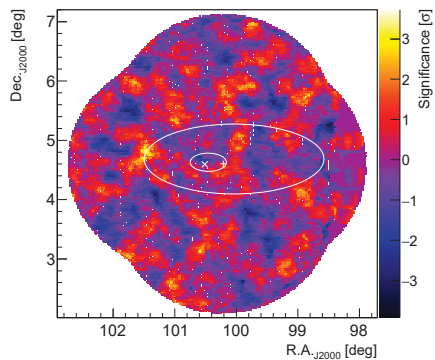
IC_NU25



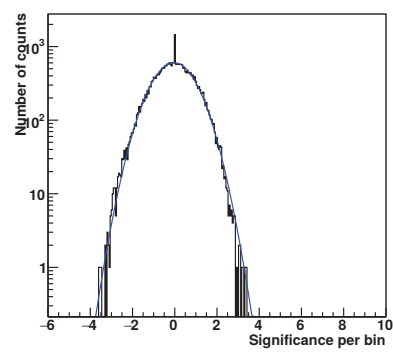
Sign Distr for All Bins



IC_NU28



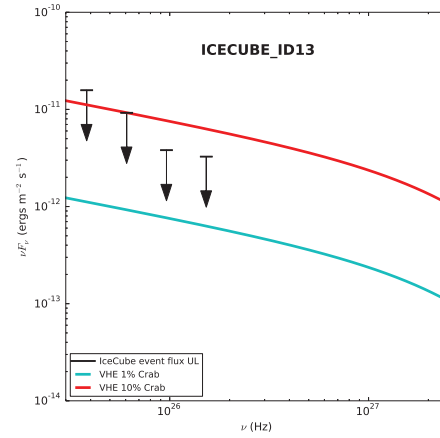
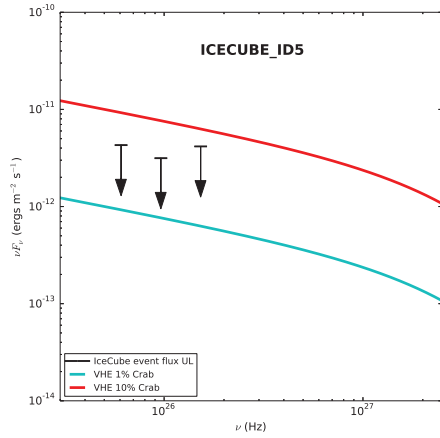
Sign Distr for All Bins

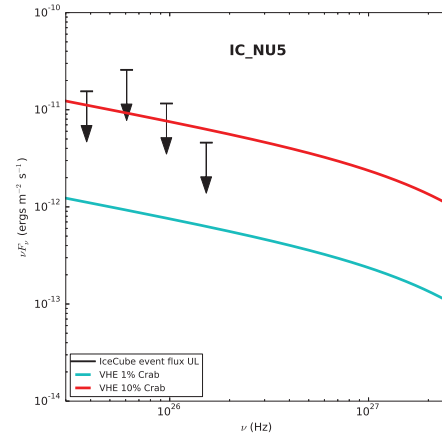
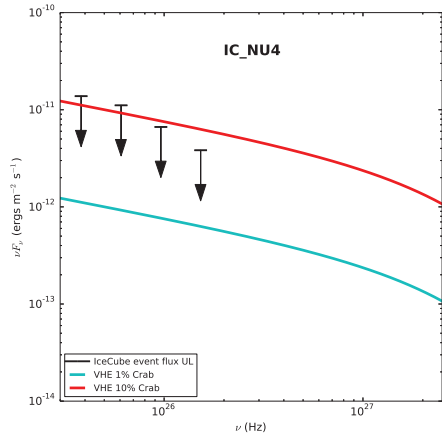
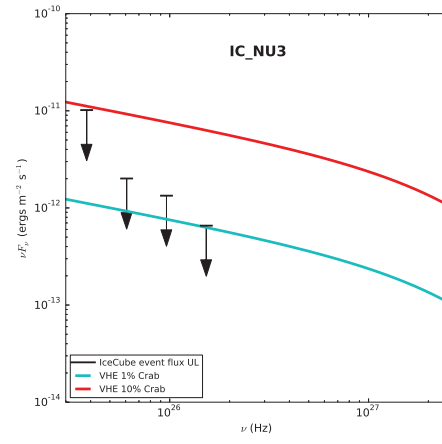
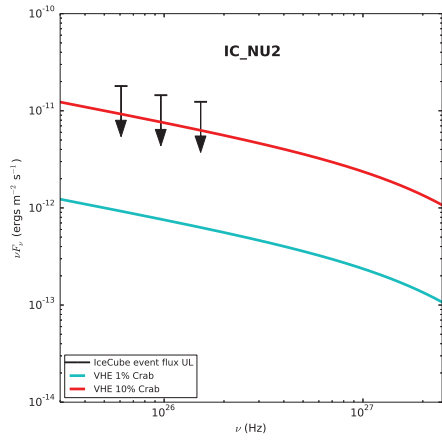
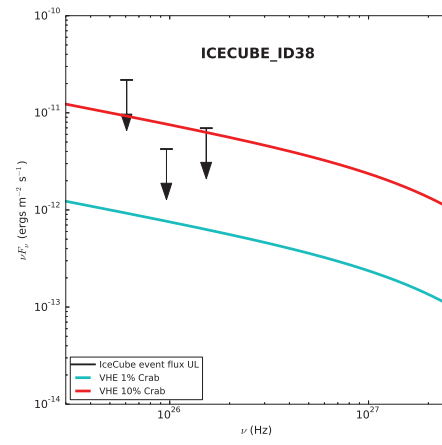
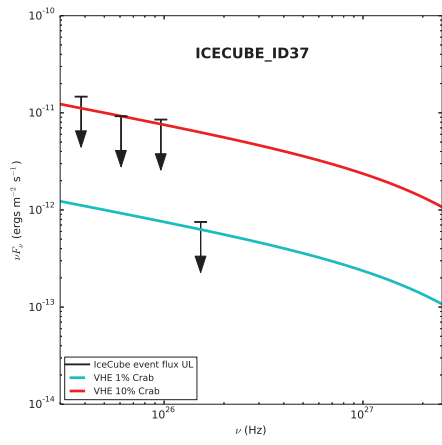


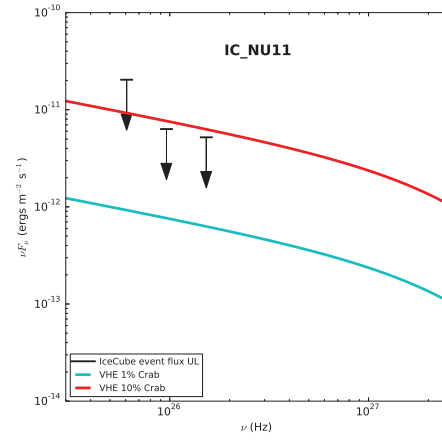
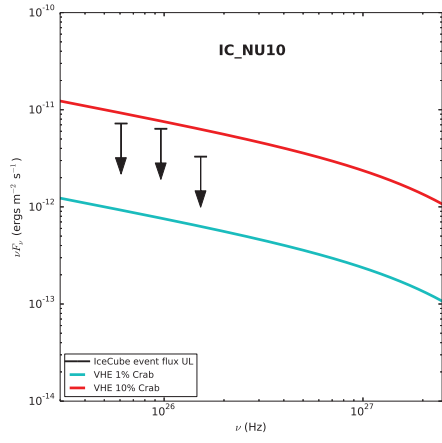
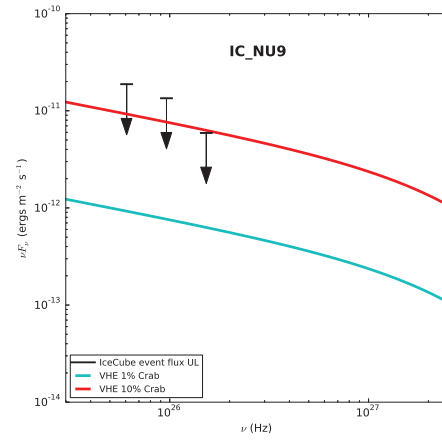
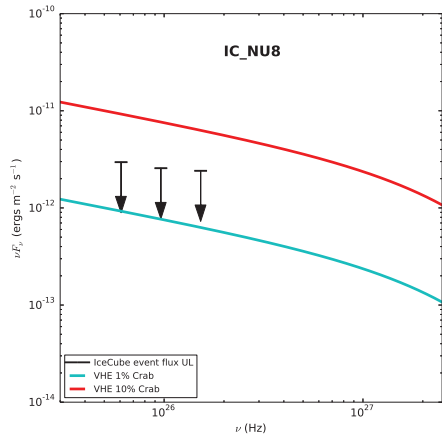
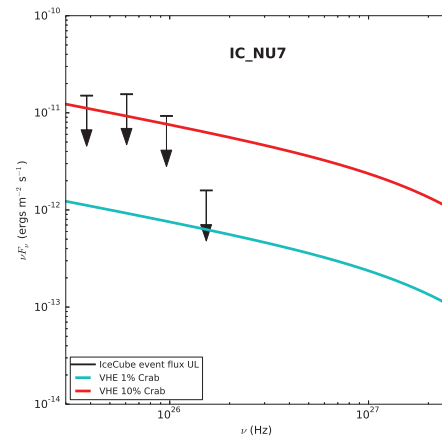
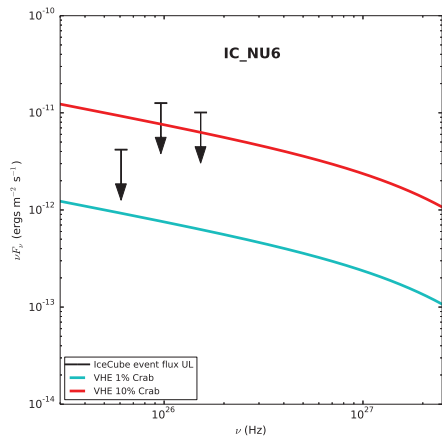
APPENDIX B

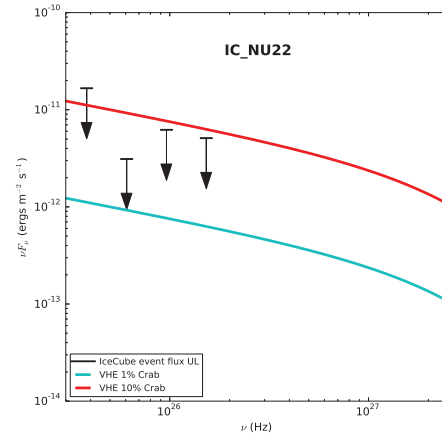
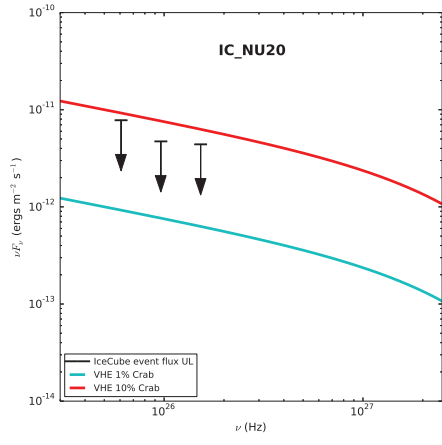
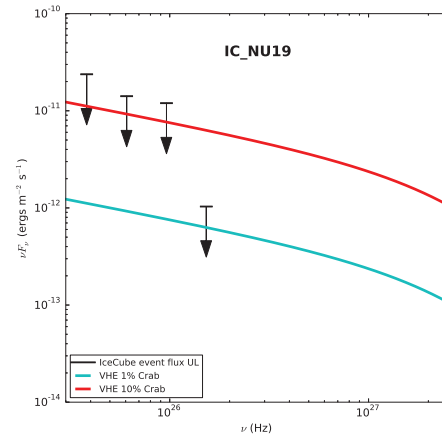
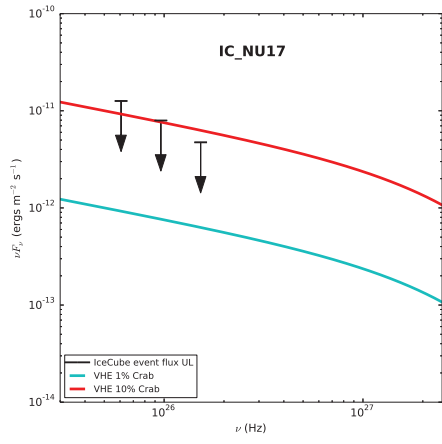
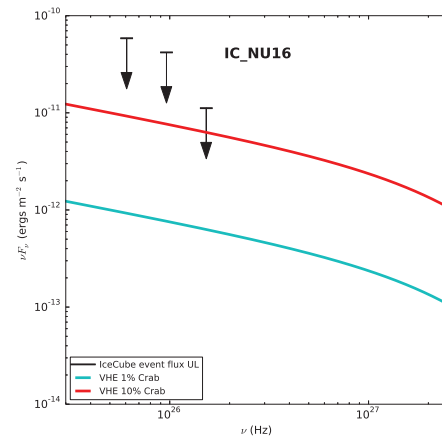
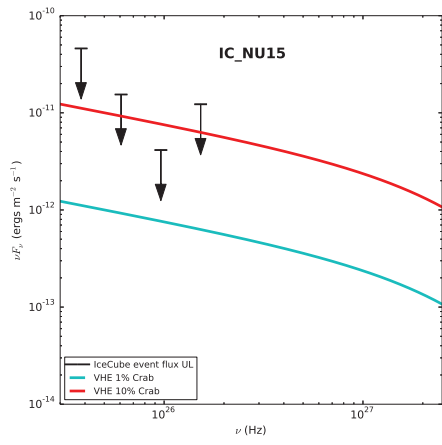
Flux upper limit spectra

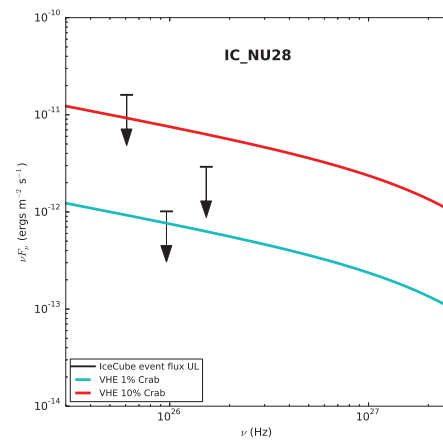
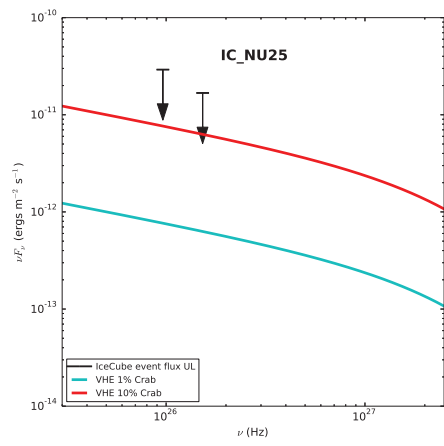
This appendix contains the spectra of gamma-ray flux upper limits calculated from VERITAS follow-up observations of IceCube neutrino events. The data was divided into 4 bins as described in Section 5.4 and the differential upper limit at the 95% confidence level was calculated for each bin. These spectra are compared with 1% and 10% Crab nebula gamma-ray flux shown here as the turquoise and red curves respectively.











References

- [1] M. G. Aartsen et al. Observation of High-Energy Astrophysical Neutrinos in Three Years of IceCube Data. *Phys. Rev. Lett.*, 113:101101, 2014.
- [2] M. G. Aartsen et al. Search for a diffuse flux of astrophysical muon neutrinos with the IceCube 59-string configuration. *Phys. Rev.*, D89(6):062007, 2014.
- [3] M. G. Aartsen et al. Evidence for Astrophysical Muon Neutrinos from the Northern Sky with IceCube. *Phys. Rev. Lett.*, 115(8):081102, 2015.
- [4] M. G. Aartsen et al. The IceCube Neutrino Observatory - Contributions to ICRC 2015 Part II: Atmospheric and Astrophysical Diffuse Neutrino Searches of All Flavors. In *Proceedings, 34th International Cosmic Ray Conference (ICRC 2015): The Hague, The Netherlands, July 30-August 6, 2015*, 2015.
- [5] M. G. Aartsen et al. Observation and Characterization of a Cosmic Muon Neutrino Flux from the Northern Hemisphere using six years of IceCube data. *Astrophys. J.*, 833(1):3, 2016.
- [6] M. G. Aartsen et al. All-sky Search for Time-integrated Neutrino Emission from Astrophysical Sources with 7 yr of IceCube Data. *Astrophys. J.*, 835(2):151, 2017.
- [7] M. G. Aartsen et al. Constraints on Galactic Neutrino Emission with Seven Years of IceCube Data. 2017.
- [8] M. G. Aartsen et al. Neutrinos and Cosmic Rays Observed by IceCube. 2017.
- [9] M. G. Aartsen et al. Search for astrophysical sources of neutrinos using cascade events in IceCube. 2017.
- [10] M. G. Aartsen et al. The IceCube Neutrino Observatory: Instrumentation and Online Systems. *Journal of Instrumentation*, 12:P03012, March 2017.
- [11] R. Abbasi et al. The IceCube Data Acquisition System: Signal Capture, Digitization, and Timestamping. *Nucl. Instrum. Meth.*, A601:294–316, 2009.

- [12] R. Abbasi et al. Calibration and characterization of the IceCube photomultiplier tube. *Nuclear Instruments and Methods in Physics Research A*, 618:139–152, June 2010.
- [13] B. P. Abbott et al. Gw170817: Observation of gravitational waves from a binary neutron star inspiral. *Phys. Rev. Lett.*, 119:161101, Oct 2017.
- [14] B. S. Acharya et al. Science with the Cherenkov Telescope Array. 2017.
- [15] E. N. Alekseev et al. Possible Detection of a Neutrino Signal on 23 February 1987 at the Baksan Underground Scintillation Telescope of the Institute of Nuclear Research. *JETP Lett.*, 45:589–592, 1987. [739(1987)].
- [16] R. M. Bionta et al. Observation of a neutrino burst in coincidence with supernova 1987a in the large magellanic cloud. *Phys. Rev. Lett.*, 58:1494–1496, Apr 1987.
- [17] IceCube collaboration. (IceCube website. <http://icecube.wisc.edu/>).
- [18] James W. Cronin. Ultra high energy cosmic rays: The pierre auger observatory. *AIP Conference Proceedings*, 566(1):1–10, 2001.
- [19] John M. Davies and Eugene S. Cotton. Design of the quartermaster solar furnace. *Solar Energy*, 1(2):16 – 22, 1957. The Proceedings of the Solar Furnace Symposium.
- [20] David J. Fegan. γ /hadron separation at TeV energies. *Journal of Physics G: Nuclear and Particle Physics*, 23(9):1013, 1997.
- [21] Stefano Gabici and Felix Aharonian. Gamma-ray emission from young supernova remnants: hadronic or leptonic? *EPJ Web Conf.*, 121:04001, 2016.
- [22] Sean Griffin. *The VERITAS Bright Moonlight Program*. PhD thesis, McGill University, 2015.
- [23] A. M. Hillas. Cerenkov light images of EAS produced by primary gamma. In F. C. Jones, editor, *International Cosmic Ray Conference*, volume 3 of *International Cosmic Ray Conference*, pages 445–448, August 1985.
- [24] K. Hirata et al. Observation of a neutrino burst from the supernova sn1987a. *Phys. Rev. Lett.*, 58:1490–1493, Apr 1987.
- [25] J. Holder. Atmospheric Cherenkov Gamma-ray Telescopes. *ArXiv e-prints*, October 2015.

- [26] J. Holder et al. (The VERITAS collaboration). The first VERITAS telescope. *Astroparticle Physics*, 25(6):391 – 401, 2006.
- [27] T.-P. Li and Y.-Q. Ma. Analysis methods for results in gamma-ray astronomy. *The Astrophysical Journal*, 272:317–324, September 1983.
- [28] John Linsley. Evidence for a primary cosmic-ray particle with energy 10^{20} ev. *Phys. Rev. Lett.*, 10:146–148, Feb 1963.
- [29] Andrew McCann. *Discovery of Emission above 100 GeV from The Crab Pulsar With VERITAS*. PhD thesis, McGill University, 2011.
- [30] P. Meszaros. *Astrophysical Sources of High Energy Neutrinos in the IceCube Era*. 2017.
- [31] A. Nepomuk Otte and for the VERITAS Collaboration. The Upgrade of VERITAS with High Efficiency Photomultipliers. *ArXiv e-prints*, October 2011.
- [32] Dan Noyes. (CERN website. <https://home.cern/about/updates/2012/08/cosmic-rays-discovered-100-years-ago>).
- [33] K. A. Olive et al. Review of Particle Physics. *Chin. Phys.*, C38:090001, 2014.
- [34] Irene Di Palma, Dafne Guetta, and Elena Amato. Revised predictions of neutrino fluxes from Pulsar Wind Nebulae. *Astrophys. J.*, 836(2):159, 2017.
- [35] Wolfgang A. Rolke, Angel M. Lopez, and Jan Conrad. Limits and confidence intervals in the presence of nuisance parameters. *Nucl. Instrum. Meth.*, A551:493–503, 2005.
- [36] G.E. Romero, V. Bosch-Ramon, J.M. Paredes, and M. Orellana. *Gamma-Ray Emission from Microquasars: Leptonic vs. Hadronic Models*, pages 480–482. Springer Berlin Heidelberg, Berlin, Heidelberg, 2007.
- [37] S. Wakely and D. Horan. (TeVCat website. <http://tevcat2.uchicago.edu/>).
- [38] Trevor C. Weekes. The Atmospheric Cerenkov imaging technique for very high energy gamma-ray astronomy. In *International WE - Heraeus Summer School: Physics with Cosmic Accelerators Bad Honnef, Germany, July 5-16, 2004*, 2005.